J. Fluid Mech. (2019), *vol.* 859, *pp.* 754–789. © Cambridge University Press 2018
doi:10.1017/jfm.2018.816

Three-dimensional direct numerical simulation of infrasound propagation in the Earth's atmosphere

R. Sabatini[1,2,3,†], O. Marsden[1], C. Bailly[1] and O. Gainville[2]

[1]Laboratoire de Mécanique des Fluides et d'Acoustique, Unité mixte de recherche CNRS 5509, École Centrale de Lyon, 69134 Écully CEDEX, France

[2]CEA, DAM, DIF, F-91297 Arpajon, France

[3]Department of Physical Sciences, Embry-Riddle Aeronautical University, Daytona Beach, FL 32114, USA

(Received 22 May 2018; revised 8 October 2018; accepted 8 October 2018)

A direct numerical simulation of the three-dimensional unsteady compressible Navier–Stokes equations is performed to investigate the infrasonic field generated in a realistic atmosphere by an explosive source placed at ground level. To this end, a high-order finite-difference method originally developed for aeroacoustic applications is employed. The maximum overpressure and the main frequency of the signal recorded at 4 km distance from the source location are about 4000 Pa and 0.2 Hz, respectively. The atmosphere is parametrized as a vertically stratified medium, constructed by specifying vertical profiles of the temperature and the horizontal wind which reproduce measurements. The computation is carried out up to 140 km altitude and 450 km range. The goal of the present paper is twofold. On the one hand, the feasibility of using a direct numerical simulation of the three-dimensional fluid dynamic equations for the detailed description of long-range propagation in the atmosphere is proven. On the other hand, a physical analysis of the infrasonic field is realized. In particular, great attention is directed towards some important phenomena which are not taken into account or not well predicted by classical propagation models. To begin with, the present study clearly demonstrates that the weakly nonlinear ray theory may lead to an incorrect evaluation of the waveform distortion of high-amplitude waves propagating towards the lower thermosphere. In addition, signals recorded in the shadow zones are investigated. In this regard, the influence on the acoustic field of temperature and wind inhomogeneities of length scale comparable with the acoustic wavelength is analysed. The role of diffraction at the thermospheric caustic is finally examined and it is pointed out that the amplitude of the source may have a strong impact on the length of the shadow zone.

Key words: acoustics, computational methods, Navier–Stokes equations

† Email address for correspondence: roberto87sabatini@gmail.com

1. Introduction

Infrasound is formally defined as sound of frequency lower than about 20 Hz, the limit of the human hearing range. Infrasonic waves are generated by a large variety of natural events, such as volcanic eruptions or earthquakes, and by artificial sources, like nuclear or chemical explosions and supersonic booms. Following particular paths which extend up to thermospheric altitudes, they can propagate over thousands of kilometres through the Earth's atmosphere and may carry relevant information about their source.

One of the earliest investigations on long-range propagation dates back to the immediate aftermath of the Krakatoa eruption in 1883 (Evers & Haak 2010). During the first four decades of the 20th century, infrasound studies were essentially motivated by the interest in the layered structure of the atmosphere. The outbreak of the Cold War probably marked the beginning of the modern era of the research in low-frequency acoustics. Thenceforth, infrasonic recordings have been extensively used to monitor the Earth for clandestine nuclear tests and constitute today one of the four techniques used by the International Monitoring System (IMS) to verify compliance with the Comprehensive Nuclear Test Ban Treaty (Brachet *et al.* 2010). The infrasound network of the IMS, still under construction, will ultimately include 60 stations which can detect frequencies roughly between 0.01 and 4 Hz. Its primary goal is to allow a reliable estimation of the source yield of large explosions. Nonetheless, a number of new practical applications where infrasound recordings may prove to be useful are currently emerging. To name a few examples, retrieval techniques for the vertical profiles of the speed of sound and wind velocity (Le Pichon *et al.* 2006; Lalande *et al.* 2012; Assink *et al.* 2013, 2014; Chunchuzov *et al.* 2015) have been recently developed; investigations on atmospheric gravity waves have been performed as well. A detailed review can be found in Le Pichon, Blanc & Hauchecorne (2010).

1.1. *Physical phenomena affecting infrasound propagation*

Infrasound propagation is primarily driven by the vertical gradients of the speed of sound and atmospheric wind, which trap the acoustic energy between the Earth's surface and the thermosphere. Tropospheric, stratospheric and thermospheric ducts are generally observed (Drob, Picone & Garcés 2003). Furthermore, the refraction induced by the variations with altitude of the propagation velocity leads to the formation of focusing regions or caustics and shadow zones (Pierce 1985). Signals travelling in the atmosphere undergo a phase shift when grazing a caustic, so that an initially N-shaped waveform, typical of an explosive source, is transformed into a U-wave (Rogers & Gardner 1980; Pierce 1985; Marchiano, Coulouvrat & Grenon 2003). Diffraction at a caustic also plays an important role, especially for low-frequency waves (Pierce 1985; Salomons 1998; Marchiano *et al.* 2003). The atmospheric stratification imposed by the gravity force has a considerable impact on acoustic propagation. The roughly exponential reduction with altitude of the mean atmospheric density indeed tends to amplify nonlinearities, which leads to signal steepening and lengthening (Rogers & Gardner 1980; Lonzaga *et al.* 2015; Sabatini *et al.* 2016*b*). Likewise, thermoviscous absorption augments as the mean atmospheric density diminishes, due to the increase of the mean kinematic viscosity (Sutherland & Bass 2004). Relaxation phenomena may also damp infrasonic waves, in particular those propagating in the troposphere and in the stratosphere (Sabatini *et al.* 2016*b*). Moreover, acoustic energy can be scattered by fine-scale temperature and wind inhomogeneities generated by internal gravity waves (Kulichkov 2004; Chunchuzov *et al.* 2011; Chunchuzov, Kulichkov &

Firstov 2013; Chunchuzov *et al.* 2014, 2015). Finally, the roughness of the Earth's surface may also alter infrasonic recordings, especially near the source (Lacanna & Ripepe 2013; de Groot-Hedlin 2017).

1.2. *Numerical modelling of infrasound propagation*

Given the complexity of the physics to be taken into account, numerical simulations of atmospheric propagation have necessarily been based on simplified approaches. Ray tracing (Rogers & Gardner 1980; Lonzaga *et al.* 2015; Sabatini *et al.* 2016*b*; Scott, Blanc-Benon & Gainville 2017), normal modes (Waxler 2002, 2004; Bertin, Millet & Bouche 2014; Assink, Waxler & Velea 2017; Waxler, Assink & Velea 2017) and one-way models (Lingevitch, Collins & Siegmann 1999; Ostashev *et al.* 2001; Le Pichon, Ceranna & Vergoz 2012; Gallin *et al.* 2014) have been the most commonly used techniques. Albeit computationally efficient, they are not able to account for all the aforementioned physical phenomena. Ray theory is valid up to the weakly nonlinear regime and does not predict by its own nature scattering by inhomogeneities and diffraction; a normal mode expansion is only admitted by linear waves in a stratified medium; finally, one-way models have strong angular limitations and are generally restricted to linear or weakly nonlinear propagation.

Over the past decade, significant efforts have been made towards infrasound studies based on the complete set of the fluid dynamic equations, for providing a finer description of long-range atmospheric propagation. However, their accurate resolution is still a challenging task and requires well-suited numerical techniques. To the best of the authors' knowledge, numerical simulations of such equations have generally been performed in two dimensions, on Cartesian grids (de Groot-Hedlin, Hedlin & Walker 2011; Marsden, Bailly & Bogey 2014; Sabatini *et al.* 2015, 2016*a*) or in cylindrical coordinates under the hypothesis of axial symmetry (de Groot-Hedlin 2012, 2016). A three-dimensional computation, based on simplified equations, was carried out by Del Pino *et al.* (2009), however without including nonlinear, viscous and thermal conduction effects.

1.3. *Present study*

In this work, the full three-dimensional unsteady compressible Navier–Stokes equations are solved in order to investigate the infrasonic field generated by an explosive source placed at ground level in a realistic atmosphere. For this purpose, a high-order finite-difference time-domain method originally developed for aeroacoustic applications (Bogey & Bailly 2002, 2004; Berland, Bogey & Bailly 2007) is employed, along with an adaptive shock-capturing algorithm (Bogey, Cacqueray & Bailly 2009; Sabatini *et al.* 2016*a*) which allows the handling of discontinuities. The maximum overpressure and the central frequency of the signal recorded at 4 km distance from the source location are about 4000 Pa and 0.2 Hz, respectively. The atmosphere is defined as a vertically stratified medium and is constructed by specifying vertical profiles of the temperature and the horizontal wind which partly reproduce the data observed during the Misty-Picture experiment (Gainville *et al.* 2010). The computation is carried out up to 140 km altitude and 450 km range.

The aim of this work is twofold. On the one hand, the feasibility of using a direct numerical simulation of the three-dimensional fluid dynamic equations for the detailed description of long-range propagation in the atmosphere is proven. On the other hand, a fine physical analysis of the infrasonic field is realized. In particular, great attention is directed towards different important phenomena which are not taken into account

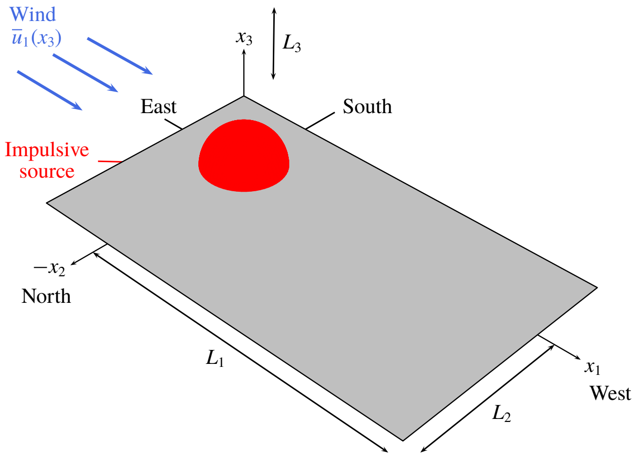

FIGURE 1. (Colour online) Sketch of the physical domain.

or not well predicted by classical propagation models, namely: the strong nonlinear effects in the thermosphere, the penetration of acoustic energy in the shadow zone on the Earth's surface, the partial reflections induced by small-scale temperature and wind inhomogeneities and the diffraction at the thermospheric caustic.

The paper is organized as follows. The present propagation model is described in § 2. The properties of the atmospheric gas and the initial mean flow are first defined. The set of governing equations and the infrasonic source are then presented and a discussion of the main hypothesis of the model is carried out. The numerical algorithm and its computer implementation are outlined in § 3. Results are finally reported in § 4. After a general illustration of the acoustic field at various instants of time, time signals at different altitudes and at ground level are examined. In particular, the nonlinear effects in the thermosphere, the penetration of acoustic energy in the shadow zone at ground level, the influence of fine-scale temperature and wind inhomogeneities and the diffraction at the thermospheric caustic are discussed. Concluding remarks are finally presented in § 5.

2. Propagation model

A Cartesian coordinate system $Ox_1x_2x_3$ with its origin at ground level and vertical axis x_3 is employed. The Earth's surface is modelled as a perfectly reflecting flat wall, which is represented by the x_1–x_2 plane. An infrasonic source is placed at the point O. A sketch of the problem is illustrated in figure 1.

2.1. *Fluid model*

For the purpose of the present investigation, the air in the atmosphere is assumed to behave as a single ideal gas satisfying the equation of state $p=\rho rT$, where p is the pressure, ρ is the fluid density, T is the temperature and $r=287.06$ J kg^{-1} K^{-1} is the specific gas constant. The speed of sound c is given by the relation $c=\sqrt{\gamma rT}$, where $\gamma=c_p/c_v=1.4$ represents the ratio of the specific heat capacity at constant pressure c_p to the specific heat capacity at constant volume $c_v=c_p-r$. The molar mass and the specific heats are considered constant. As a result, the internal energy e and the enthalpy h are simply computed as $e=c_vT$ and $h=c_pT$, respectively. The fluid

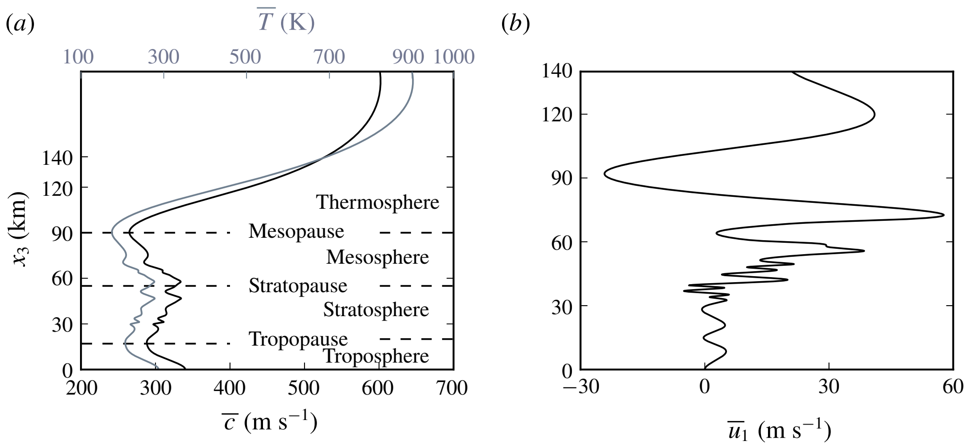

FIGURE 2. (a) Vertical profiles of the speed of sound $\bar{c}(x_3)$ (black line) and of the temperature $\bar{T}(x_3)$ (grey line); (b) mean horizontal wind $\bar{u}_1(x_3)$ in the east–west direction versus altitude.

flow is described by the conservative variables $[\rho, \rho u_1, \rho u_2, \rho u_3, \rho e_t]$, where u_i is the component of the velocity vector in the direction x_i, for $i = 1, 2, 3$, and $e_t = e + u_k u_k/2$ indicates the total specific energy, which is related to the pressure p by the relationship $p = (\gamma - 1)(\rho e_t - \rho u_k u_k/2)$.

2.2. *Initial undisturbed atmosphere*

At the instant $t = 0$, the initial undisturbed atmosphere is defined as a stationary and stratified medium, with a wind in the x_1 direction

$$\bar{\rho} = \bar{\rho}(x_3), \quad \bar{\rho}\bar{u}_i = \bar{\rho}(x_3)\bar{u}_i(x_3), \quad i = 1, 2, 3, \quad \bar{\rho}\bar{e}_t = \bar{\rho}(x_3)\bar{e}_t(x_3). \qquad (2.1a–c)$$

In the present study, the vertical profiles of the temperature $\bar{T}(x_3)$ and the horizontal wind $\bar{u}_1(x_3)$ are defined by combining the data measured during the Misty-Picture experiment with empirical models (see Gainville *et al.* (2010) for further details). They are displayed in figures 2(a) and 2(b), respectively. A synthetic nomenclature of the different atmospheric layers is also reported in figure 2(a). The length scale for variations of the initial undisturbed atmosphere is globally higher than around 10 km. Nonetheless, small-scale inhomogeneities are clearly visible in the stratosphere, between 25 and 55 km altitude. Their characteristic length is equal to about 4 km and is close to the acoustic wavelengths λ considered in this study.

The mean speed of sound $\bar{c}(x_3)$ is computed from the temperature according to the relation $\bar{c}(x_3) = \sqrt{\gamma r \bar{T}(x_3)}$. The pressure profile $\bar{p}(x_3)$ is then obtained by integrating the hydrostatic equilibrium equation

$$\frac{d\bar{p}}{dx_3} = -\bar{\rho} g = -\frac{g}{r\bar{T}}\bar{p}, \qquad (2.2)$$

where $g = 9.81$ m s^{-2} is the gravitational acceleration, here assumed to be constant, with the ground-level pressure fixed to $\bar{p}_0 \equiv \bar{p}(0) = 101\,325$ Pa. Finally, the density and the specific energy are determined from the expressions $\bar{\rho} = \bar{p}/(r\bar{T})$ and $\bar{\rho}\bar{e}_t = \bar{p}/(\gamma - 1) + \bar{\rho}\bar{u}_1^2/2$.

2.3. *Governing equations*

Sound propagation is governed by the three-dimensional unsteady compressible Navier–Stokes equations, which can be recast as

$$\left.\begin{aligned}\frac{\partial\rho}{\partial t}+\frac{\partial(\rho u_j)}{\partial x_j}&=\Lambda_\rho,\\ \frac{\partial(\rho u_i)}{\partial t}+\frac{\partial(\rho u_i u_j)}{\partial x_j}&=-\frac{\partial p'}{\partial x_i}+\frac{\partial\tau^\star_{ij}}{\partial x_j}-\rho' g\delta_{i3},\\ \frac{\partial(\rho e_t)}{\partial t}+\frac{\partial(\rho e_t u_j)}{\partial x_j}&=-\frac{\partial\left(p'u_j\right)}{\partial x_j}-\bar{p}\frac{\partial u_j}{\partial x_j}-\frac{\partial q^\star_j}{\partial x_j}+\frac{\partial(u_i\tau^\star_{ij})}{\partial x_j}-\rho' g u_3+\Lambda_{\rho e_t},\end{aligned}\right\}\tag{2.3}$$

where $p'=p-\bar{p}$ is the pressure perturbation, $\rho'=\rho-\bar{\rho}$ is the density perturbation, $\tau^\star_{ij}$ is the viscous stress tensor, q'_i is the heat flux, Λ_ρ and $\Lambda_{\rho e_t}$ are two source-forcing terms and δ_{ij} is the Kronecker symbol. Note that, in keeping with Marsden *et al.* (2014), the hydrostatic equilibrium condition $\mathrm{d}\bar{p}/\mathrm{d}x_3=-\bar{\rho}g$ is here subtracted from the Navier–Stokes equations in order to bypass its high-precision computation at each time step. Moreover, because of the non-vanishing terms $\partial\bar{\tau}_{12}/\partial x_1$ and $\partial\bar{q}_2/\partial x_2$, the initial undisturbed atmosphere, determined from experimental data, is not fully consistent with the Navier–Stokes equations and thus would tend to evolve in time. To avoid the diffusion of the mean flow during the acoustic propagation, the viscous and the thermal conduction terms are calculated using the perturbed variables $u'_i=u_i-\bar{u}_i$ and $T'=T-\bar{T}$. More specifically, the viscous stress tensor and the heat flux are computed respectively as

$$\tau^\star_{ij}=\mu\left(\frac{\partial u'_i}{\partial x_j}+\frac{\partial u'_j}{\partial x_i}-\frac{2}{3}\frac{\partial u'_k}{\partial x_k}\delta_{ij}\right)\tag{2.4}$$

and

$$q^\star_i=-\frac{\mu c_p}{Pr}\frac{\partial T'}{\partial x_i},\tag{2.5}$$

where μ is the dynamic viscosity and $Pr=0.72$ is the fluid's Prandtl number. Finally, the dynamic viscosity is given by the expression

$$\mu(T)=\mu_{ref}\left(\frac{T}{T_{ref}}\right)^{3/2}\frac{T_{ref}+T_S}{T+T_S},\tag{2.6}$$

where $\mu_{ref}=1.8192\times10^{-5}$ Pa s, $T_{ref}=293.15$ K and $T_S=117$ K (Sutherland & Bass 2004, 2006).

2.4. *Infrasonic source*

The infrasonic source is implemented through the following forcing terms of the continuity and energy conservation equations:

$$\left.\begin{aligned}\Lambda_{\rho e_t}(\boldsymbol{x},t)&=\mathcal{A}_s\sin(\omega_s t)[1-\cos(2\omega_s t)]\Pi_{[0,\pi/\omega_s]}(t)\mathrm{e}^{-\log(2)\|\boldsymbol{x}\|^2/b_s^2}\\ \Lambda_\rho(\boldsymbol{x},t)&=\frac{\gamma-1}{\bar{c}^2(x_3)}\Lambda_{\rho e_t}(\boldsymbol{x},t),\end{aligned}\right\}\tag{2.7}$$

where $\mathcal{A}_s=3\times10^5$ J m^{-3} s^{-1} is the source strength, $f_s=\omega_s/(2\pi)=0.2$ Hz the source frequency, $b_s=360$ m the half-width and $\Pi_{[0,\pi/\omega_s]}(t)$ the rectangle function, equal to 1 in the interval $[0,\pi/\omega_s]$ and 0 otherwise. As explained in appendix A, the functions $\Lambda_{\rho e_t}$ and Λ_ρ are designed in order to obtain a blast wave, typical of explosions (Whitham 1974), close to the origin of the domain.

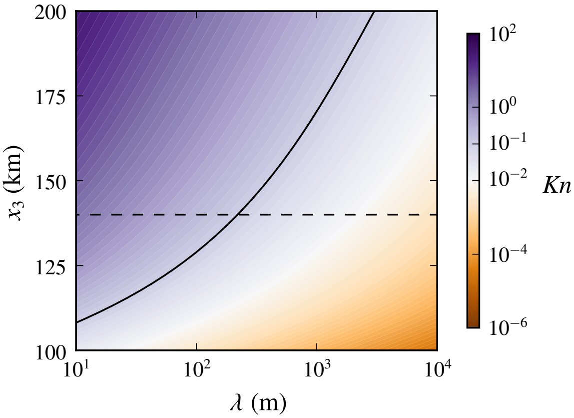

FIGURE 3. (Colour online) Knudsen number Kn as a function of the wavelength λ and of the altitude x_3. The solid and dashed lines represent the level set $Kn = 0.1$ and the limit of the physical domain of interest, respectively.

2.5. *About the main hypotheses of the present propagation model*

The present propagation model, based on the three-dimensional compressible unsteady Navier–Stokes equations, rests upon the continuum hypothesis (Batchelor 2012), which is valid when the characteristic wavelength λ is large enough compared to the free mean path ℓ. This latter is equal to about 10^{-7} m at ground level, but can reach significant values in the thermosphere. The typical behaviour of the Knudsen number $Kn = \ell/\lambda$ in the atmosphere is shown in figure 3 as a function of the wavelength λ and of the altitude x_3. The conventional limit of validity, $Kn = 0.1$, is also reported. Clearly, becoming irrelevant at altitudes higher than 140 km for values of λ lower than about 200 m, the continuum hypothesis is verified for the range of wavelengths of interest in this study.

Another underlying assumption of the present model is the negligibility of relaxation effects, but, as shown by Sabatini *et al.* (2016*b*), non-equilibrium phenomena mainly affect tropospheric and stratospheric waves of frequency greater than 1 Hz.

3. Numerical algorithm

System (2.3) is solved on a Cartesian grid using a high-order finite-difference time-domain method.

3.1. *Computational domain*

The maximum number of mesh points being constrained by the computer memory, a moving frame is employed (Salomons, Blumrich & Heimann 2002; Sabatini *et al.* 2015; de Groot-Hedlin 2016). System (2.3) is solved only in a narrow region which moves along the x_1 axis and follows the acoustic wavefront. A schematic illustration of the technique is provided in figure 4(*a*). The physical domain of interest is a parallelepiped of sizes 450 km, $L_2^{phys} = 90$ km, $L_3^{phys} = 140$ km along the x_1, x_2, x_3 axes, respectively, while the moving window covers a distance of $L_1^{phys} = 220$ km in the x_1 direction. As displayed in figures 5(*a*) and 5(*b*), the physical domain $L_1^{phys} \times L_2^{phys} \times L_3^{phys}$ is surrounded by sponge zones where particular numerical

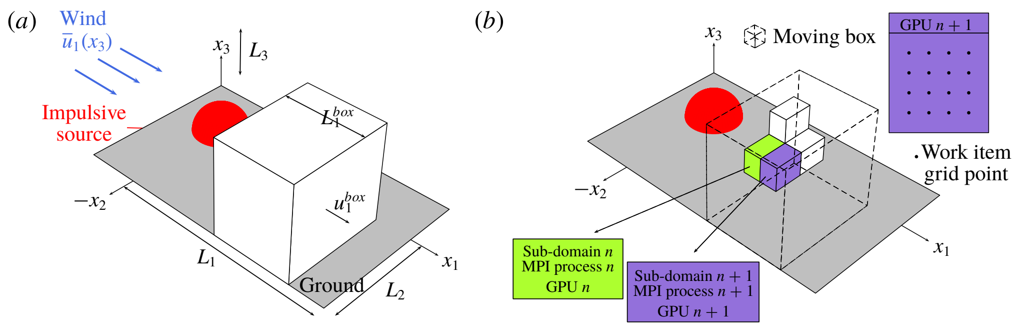

FIGURE 4. (Colour online) (*a*) Sketch of the computational domain. (*b*) Schematic illustration of the two-level parallelism of the present solver for the Navier–Stokes equations.

techniques are used in order for outgoing waves to leave the computational frame without significant reflections. Moreover, since no wind is considered in the x_2 direction and the source forcing terms (2.7) depends only on the radial distance $\|\boldsymbol{x}\|$, the acoustic field is symmetric across the x_1–x_3 plane. Accordingly, with reference to figure 4(*a*), System (2.3) is solved only for negative values of the coordinate x_2.

3.2. *Numerical schemes*

At inner points, the spatial derivatives are computed using an explicit fourth-order 11-point stencil finite-difference scheme optimized to reduce dispersion for wavelengths shorter than about five grid spacings (Bogey & Bailly 2004). Close to the boundaries of the computational domain, optimized 11-point stencil non-centred finite-difference schemes are employed (Berland *et al.* 2007). The time integration is carried out by a six-step second-order low-storage Runge–Kutta algorithm (Bogey & Bailly 2004).

At the end of each time step, spatial low pass filtering is performed on the perturbations of conservative variables $U' = [\rho - \bar{\rho}, \rho u_1 - \bar{\rho}\bar{u}_1, \rho u_2 - \bar{\rho}\bar{u}_2, \rho u_3 - \bar{\rho}\bar{u}_3, \rho e_t - \bar{\rho}\bar{e}_t]$, in order to damp out grid-to-grid oscillations and ensure numerical stability. For this purpose, an explicit sixth-order 11-point stencil filter, designed to remove fluctuations discretized by less than four grid points per wavelength, while leaving larger wavelengths unaffected, is employed at inner nodes (Bogey *et al.* 2009). Close to the boundaries of the computational frame, optimized 11-point stencil non-centred filters are applied instead (Berland *et al.* 2007). Additionally, in order to handle the acoustic shocks generated during the propagation, the shock-capturing procedure developed by Bogey *et al.* (2009) is used in conjunction with the new shock detector proposed by Sabatini *et al.* (2016*a*).

3.3. *Boundary conditions and sponge zones*

The flow field near a wall can be decomposed, in the linear regime, into the sum of three different waves, namely the vorticity, the entropy and the acoustic modes. The first two waves have appreciable amplitudes only in the vicinity of the wall, up to distances of the order of the acoustic boundary layer thickness $\delta_\mu = \sqrt{2\bar{\mu}/(2\pi f \bar{\rho})}$. Close to the Earth's surface, δ_μ is equal to about 1 cm for a frequency f of 0.2 Hz and a wavelength λ of 1.7 km, i.e. $\delta_\mu = 1.7 \times 10^{-6}\,\lambda$. Understandably, in the present simulation, the flow field at ground level is dominated by the acoustic mode, which

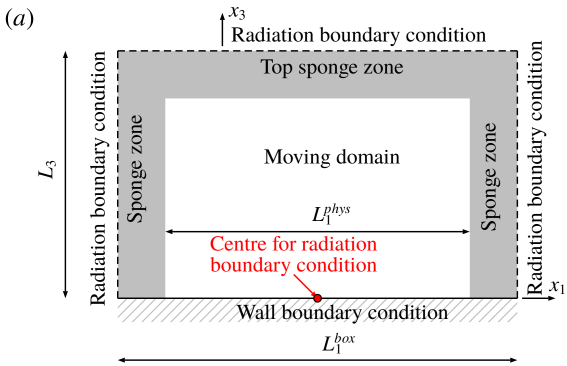

FIGURE 5. (Colour online) Projections of the moving domain on the (*a*) x_1–x_3 and (*b*) x_2–x_3 planes.

alone satisfies a no-slip boundary condition. Accordingly, at nodes on the Earth's surface, only the vertical velocity u_3 is set to zero, whereas no condition is imposed on the other conservative variables, which are advanced in time by solving the Navier–Stokes equations.

At grid points on the other boundaries, radiation conditions, as formulated by Bogey & Bailly (2002), are implemented. In order to diminish the amplitude of the outgoing waves reaching the boundaries of the computational domain, in the sponge zones, a Laplacian filter is employed. Its strength gradually augments from zero, at the beginning of the sponge layer, to a maximum value at the extremity of the frame. Along the x_2 and x_3 axes, the reduction of the wave amplitude is further enhanced by the increase of the grid spacing. A supplementary technique is finally required in the top numerical sponge zone. Due to gravity stratification, the ratio of pressure fluctuations to ambient pressure would tend to amplify with altitude. Therefore, as proposed by Marsden *et al.* (2014), the gravity profile in the top sponge layer is progressively reduced from g to $-g$.

3.4. *Informatic implementation and numerical parameters*

The numerical algorithm has been written in C/C++ with a two-level parallelism, allowing one to exploit the excellent performance of GPU clusters (Jacobsen & Senocak 2013). The moving box is split into several sub-domains, each of which is handled by an MPI process. In its turn, each MPI node drives, thanks to OpenCL kernels, a GPU. A GPU can be seen as an ensemble of work-groups, each of which is made of processing elements or work-items. The same program or kernel (such as the kernel computing the partial derivative along an axis) can be executed on all the processing elements at the same time. Hence, each work-item can handle all the operations for a single grid node (cf. figure 4*b*).

The moving box is divided into $6 \times 8 \times 3 = 144$ sub-domains, each of which contains $448 \times 64 \times 512$ grid points. The total number of mesh nodes is about 2.11 billion. The step size is constant and equal to $\Delta x_1 = 90$ m on the x_1 axis. On the x_2 axis, the grid is stretched with a rate of 0.6 % from $x_2 = 1$ km to $x_2 = 105$ km and with a rate equal to 1.2 % beyond. On the x_3 axis, the spatial step is of 90 up to 125 km, and then increases at a rate of 2 %. The variations of the mesh spacings Δx_2 and Δx_3 are represented in figures 6(*a*) and 6(*b*).

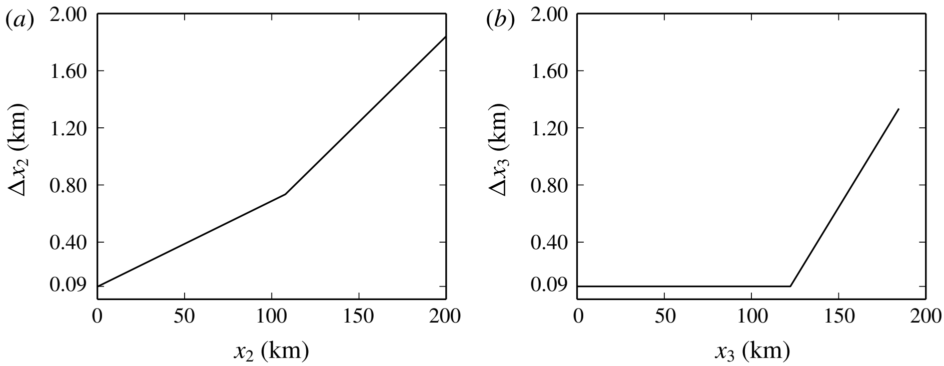

FIGURE 6. Variations of the grid spacing along (*a*) the x_2 axis and (*b*) the x_3 axis.

The time step is set equal to 0.0699 s and the computation is carried out up to 1600 s, corresponding to 23 000 iterations. The Courant–Friedrichs–Lewy and Fourier numbers computed using the speed of sound and the kinematic viscosity at the top of the physical domain along the vertical axis are 0.4 and 0.07, respectively.

The present numerical simulation was run on the hybrid nodes of the Curie supercomputer, located in the Commissariat à l'énergie atomique et aux énergies alternatives (CEA, France), and 144 Nvidia M2090 T20A GPUs were used.

4. Results

As demonstrated by Bergmann (1946), the amplitude of the pressure perturbation p' evolves proportionally to the square root of the ambient density $\bar{\rho}$. Therefore, the normalized pressure fluctuation $\Phi(\boldsymbol{x}, t) = p'(\boldsymbol{x}, t)/\sqrt{\bar{\rho}(x_3)}$ is analysed along with the overpressure p'. In addition, the signature of p' and Φ are studied in the frequency domain, by considering the one-sided energy spectral density

$$\mathcal{E}_\chi(\boldsymbol{x}, f) = 2\left|\int_{-\infty}^{+\infty} \chi(\boldsymbol{x}, t)\mathrm{e}^{\mathrm{i}2\pi ft}\,\mathrm{d}t\right|^2, \quad f \in \mathbb{R}^+, \chi = p', \Phi. \tag{4.1}$$

4.1. *General description of the acoustic field*

The three-dimensional normalized pressure fields Φ obtained at different instants of time are displayed in figure 7(*a–i*). The black box represents the computational moving frame, whereas the red box indicates the physical domain of interest. The colour level ranges from -10 Pa kg$^{-1/2}$ m$^{3/2}$ (blue) to $+10$ Pa kg$^{-1/2}$ m$^{3/2}$ (red). This interval is chosen in order to visualize the various infrasonic phases, which may have very different amplitudes. Successive points on the axes x_1, x_2 and x_3 are 100 km distant.

Near the source location, a spherical wavefront is observed. However, as a result of the vertical gradients of the speed of sound and of the horizontal wind, the infrasonic wave is continuously deformed during the propagation. At the instant t_2, partial reflections start being observed between 25 and 55 km altitude. They are induced by variations of the speed of sound and of the wind of length scale comparable to the acoustic wavelength. The amplitude of these reflections appears strengthened at the instant t_3. Moreover, because of nonlinear effects, the acoustic wavefront lengthens

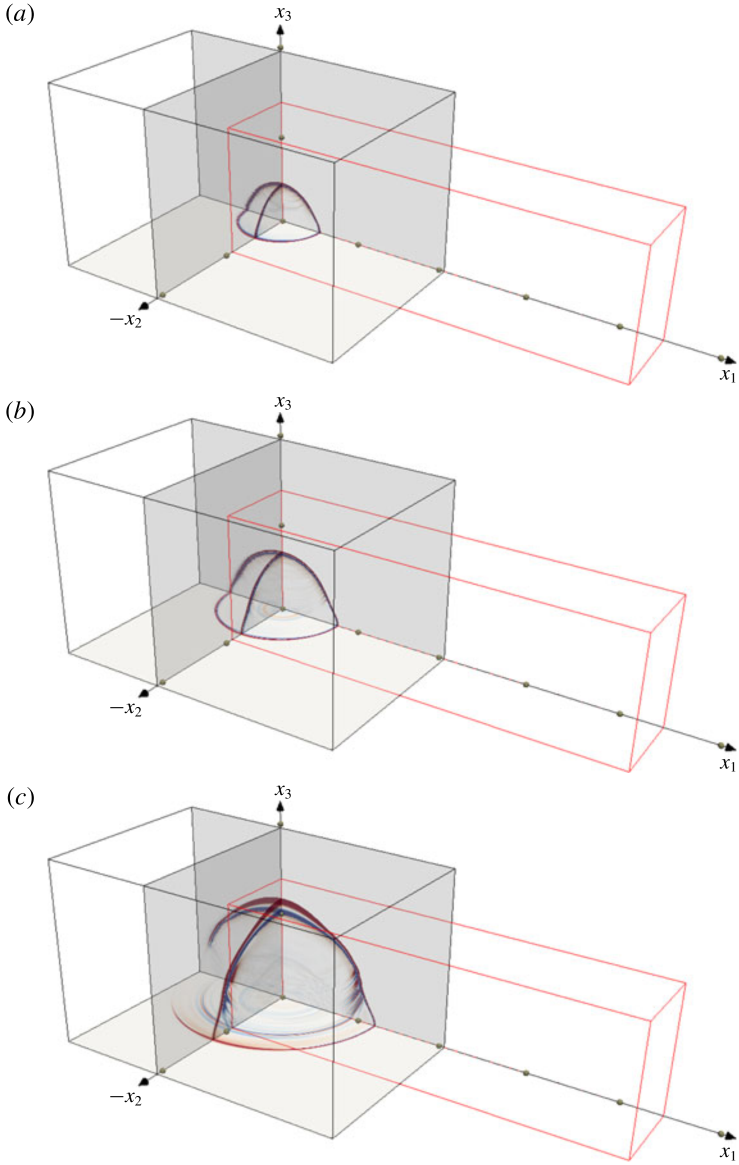

FIGURE 7. For caption see next page.

while propagating towards the thermosphere. At the instant t_4, the infrasonic wave is refracted back towards the Earth's surface. In addition, part of the wavefront leaves the domain through the top boundary. The computational frame starts moving between times t_4 and t_5. At the instant t_5, the signal at ground level, between $x_1 = 200$ km and $x_1 = 250$ km on the x_1 axis, is a superposition of partial reflections and stratospheric returns, while a thermospheric phase is reaching the Earth's surface at about $x_1 = 180$ km distance from the source location. Furthermore, part of the wavefront leaves the moving window through the plane $x_2 = -L_2$ with a negligible level of spurious reflection. At the instant t_6, the thermospheric phase is clearly visible on the ground at around $x_1 = 250$ km. At successive instants, the pressure

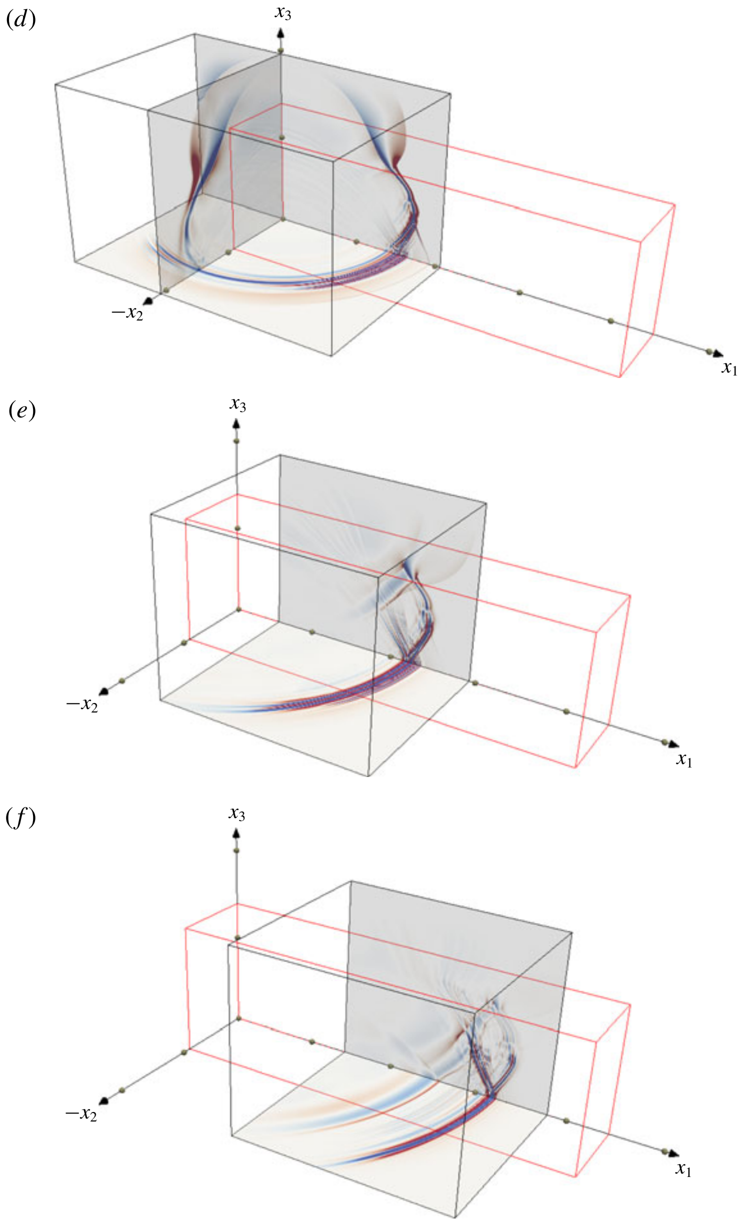

FIGURE 7 (cntd). For caption see next page.

field becomes more and more complex and a multitude of arrivals are recorded at the Earth's surface. The computational box stops moving just after reaching the boundary of the physical domain, between times t_6 and t_7. The simulation ends up once the wavefront exits the frame.

4.2. *The signal in the near field*

The pressure perturbation p' recorded on the x_1 axis at $x_1 = 7.92$ km and the corresponding energy spectral density $\mathcal{E}_{p'}$ are plotted in figure 8(*a*,*b*). The pressure

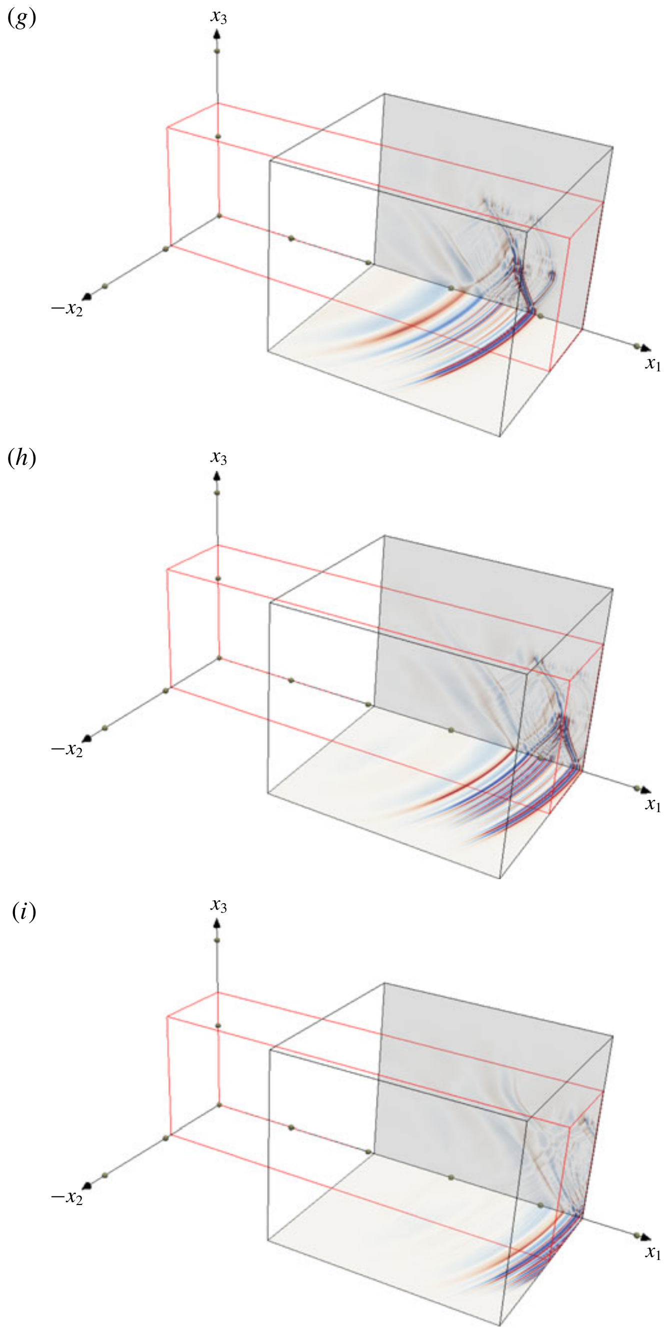

FIGURE 7 (cntd). (Colour online) Three-dimensional normalized pressure field Φ obtained for different instants of time. The black box represents the computational moving frame, whereas the red box is the physical domain of interest. The times are (*a*) $t_1 = 146.79$ s, (*b*) $t_2 = 216.69$ s, (*c*) $t_3 = 356.49$ s, (*d*) $t_4 = 566.19$ s, (*e*) $t_5 = 775.89$ s, (*f*) $t_6 = 1055.49$ s, (*g*) $t_7 = 1265.19$ s, (*h*) $t_8 = 1404.99$ s, (*i*) $t_9 = 1544.79$ s.

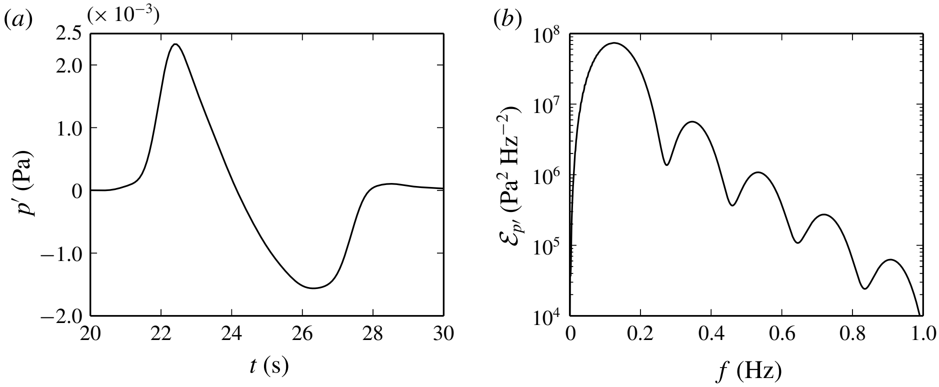

FIGURE 8. (*a*) Pressure perturbation p' recorded on the x_1 axis at $x_1 = 7.92$ km and (*b*) corresponding energy spectral density $\mathcal{E}_{p'}$.

signal in the near field exhibits an N-waveform, has a maximum amplitude of 2330 Pa and a total duration of 6 s. The central frequency is equal to about 0.13 Hz and corresponds to a wavelength of 2.6 km.

4.3. *Nonlinear effects in the upper atmosphere*

The normalized pressure perturbations Φ recorded along the vertical axis x_3 at three different altitudes are plotted in figure 9(*a–c*). At $x_3 = 50$ km, an N-shaped signal with a period of 12 s is observed. As a result of nonlinearities, the N-wave lengthens while propagating towards the upper atmosphere, its duration being equal to about 26 and 75 s at $x_3 = 90$ and 130 km altitude, respectively. A diminution of the amplitude associated with the increase of the wave period is observed as well. Moreover, at $x_3 = 130$ km, the central part of the N-wave is found to be curved. This result is in disagreement with the weakly nonlinear ray theory, according to which an N-wave should conserve its shape during the propagation. The weakly nonlinear ray theory rests upon the assumption that the amplitude of the signal p' remains at least one order of magnitude smaller than the atmospheric pressure $\bar{p}$, that is, $p' < 0.1\bar{p}$ (for instance, see Whitham (1974)). As illustrated in figure 10, where the maximum in time of the ratio $P_3(x_3, t) = p'(x_1 = 0, x_2 = 0, x_3, t)/\bar{p}(x_3)$ is plotted as a function of the altitude x_3, the hypothesis $\max_t(P_3) < 0.1$ is however not verified near the source as well as in the thermosphere. As an example, $\max_t(P_3)$ is equal to about 0.7 at $x_3 = 114$ km altitude. Therefore, the nonlinear effects cannot be considered weak in the present simulation. To the best of the authors' knowledge, a model for moderate amplitude waves in a variable atmosphere is currently not available. Qualitative insights into the understanding of the aforesaid signal distortion can nevertheless be gained through a closer analysis of the propagation of one-dimensional plane waves in a homogeneous medium at rest. First, let it be assumed that the viscous and the thermal conduction terms are negligibly small. Second, with x_3 the propagation direction, let it be supposed that the specific entropy s is constant, $s = \bar{s}$, and that the velocity $u_3 = u_3'$ is a single-valued function of the pressure p. According to Whitham (1974), the evolution of a right-running signal is then described by the following nonlinear partial differential equation:

$$\frac{\partial p'}{\partial t} + (u_3 + c)\frac{\partial p'}{\partial x_3} = 0, \tag{4.2}$$

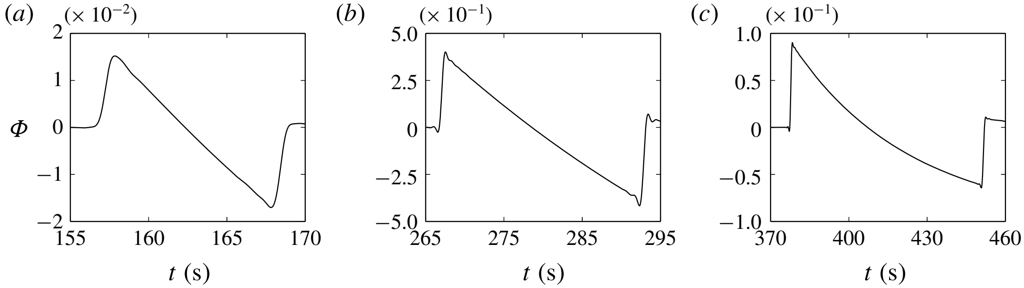

FIGURE 9. Normalized pressure signals Φ recorded on the x_3 axis at (*a*) $x_3 = 50$ km, (*b*) $x_3 = 90$ km and (*c*) $x_3 = 130$ km.

with $p = \bar{p}(\rho/\bar{\rho})^\gamma$, $c = \sqrt{\gamma p/\rho}$ and $u_3 = 2(c - \bar{c})/(\gamma - 1)$. Writing the sum $(u_3 + c)$ as a function of the pressure p and expanding it for $p'/\bar{p} \to 0$ yields

$$\frac{\partial p'}{\partial t} + \bar{c}\left[1 + \frac{\beta}{\bar{\rho}\bar{c}^2} p' - \frac{\beta^2}{2\bar{\rho}^2\bar{c}^4} p'^2 + \text{h.o.t.}\right] \frac{\partial p'}{\partial x_3} = 0, \tag{4.3}$$

where $\beta = (\gamma + 1)/2$ is the nonlinear parameter. In the presence of shock waves, the previous hypotheses on the specific entropy s and on the velocity u_3 are not verified. However, it can be shown that, at a discontinuity, the relations $s - \bar{s} = 0$ and $u_3 = u_3' = 2(c - \bar{c})/(\gamma - 1)$ are valid up to the third order in $p'/\bar{p}$ when $p'/\bar{p}$ tends to 0 (Whitham 1974). Therefore, equation (4.3) can still be employed in the presence of small or moderate amplitude shocks. When only the first two terms of the Taylor series for $(u_3 + c)$ are retained, $u_3 + c = \bar{c} + \beta p'/(\bar{\rho}\bar{c})$, the classical Burgers equation is recovered. Ray theory is entirely based on an extension of this latter equation to inhomogeneous media (for instance, see Sabatini *et al.* (2016*b*) and references therein). In the case of the Burgers equation, an N-wave conserves its shape as a consequence of the linearity in p' of the first-order approximation of $(u_3 + c)$. The central part of the waveform remains straight and only a variation of slope can be observed during the propagation. The curvature of the signals recorded in the thermosphere might be thus attributed to high-order terms in p', which cannot be neglected beyond a certain altitude. A similar discussion of the distortion of high-amplitude N-waves can be found in Inoue & Yano (1997).

The energy spectral density $\mathcal{E}_{\Phi,3}(x_3, f) = \mathcal{E}_\Phi(0, 0, x_3, f)$ of the signals Φ recorded along the x_3 axis is finally plotted in figure 11 as a function of the frequency f and of the altitude x_3. The nonlinear lengthening of the N-wave leads to a shift of the spectrum towards very low frequencies. Therefore, throughout the propagation, most of the energy is carried by spectral components which are weakly affected by the viscous and the thermal conduction terms. Dissipative effects only influence the shock region, but play a minor role in the waveform.

4.4. *Description of the arrivals at ground level*

Two waveguides are induced by the vertical profiles (2.1) of the speed of sound and of the wind, a stratospheric duct between the Earth's surface and about 55 km altitude, and a thermospheric duct between the ground and 115 km altitude. As a consequence, different arrivals reach the Earth's surface. The pressure perturbations

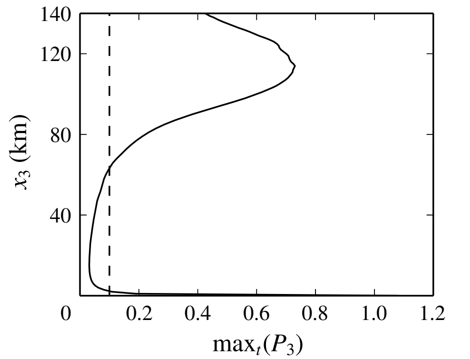

FIGURE 10. Maximum of the ratio P_3 between the pressure perturbation p' on the x_3 axis and the atmospheric pressure $\bar{p}$. The dashed line represents the conventional limit of validity of the weakly nonlinear ray theory, $\max_t(P_3) = 0.1$.

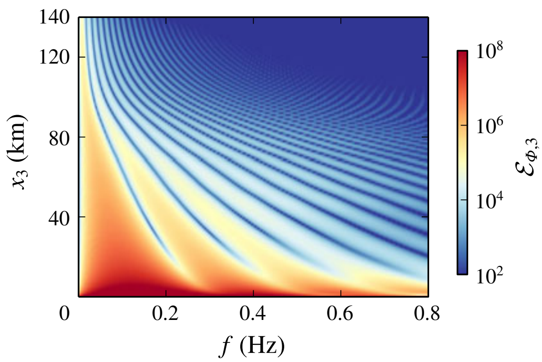

FIGURE 11. (Colour online) Spectrum $\mathcal{E}_{\Phi,3}$ of the signals Φ recorded along the x_3 axis.

p' detected on the x_1 axis at the ground stations $x_1 = 100$ km, $x_1 = 230$ km and $x_1 = 360$ km are plotted in figures 12(*b*), 12(*d*) and 12(*f*), respectively. In order to help the understanding of the various arrivals, the acoustic fields Φ obtained on the x_1–x_3 plane at times t_3, t_5 and t_7 are also displayed in figures 12(*a*), 12(*c*) and 12(*e*), respectively. The results obtained by ray theory (Candel 1977) are reported as well in figure 12(*a*,*c*). At the ground station located at $x_1 = 100$ km range, refer to figure 12(*b*), two distinct wave packets are observed. The first arrival, labelled I_{dtr}, where the subscripts d and tr stand respectively for diffracted and tropospheric, is not predicted by the geometrical acoustics approximation and may be attributed to a creeping wave which diffracts energy along the Earth's surface (Pierce 1985). It is detected between about $t = 290$ s and $t = 300$ s, its maximum overpressure is equal to 30.8 Pa and its duration is around 6 s. No period lengthening is observed, meaning that the propagation at ground level is essentially linear. An analogous conclusion has been drawn in a recent study by de Groot-Hedlin (2017). The second arrival, detected from $t = 360$ to 460 s, is associated with the partial reflections the wavefront undergoes while travelling within the small-scale inhomogeneous layer located between 25 and 55 km altitude. For this reason, it is denoted I_{ps}, where the subscripts p and s stand for partial reflection and stratospheric. Its amplitude is about 7 Pa. It can also be remarked that, at time t_1, a stratospheric return, labelled

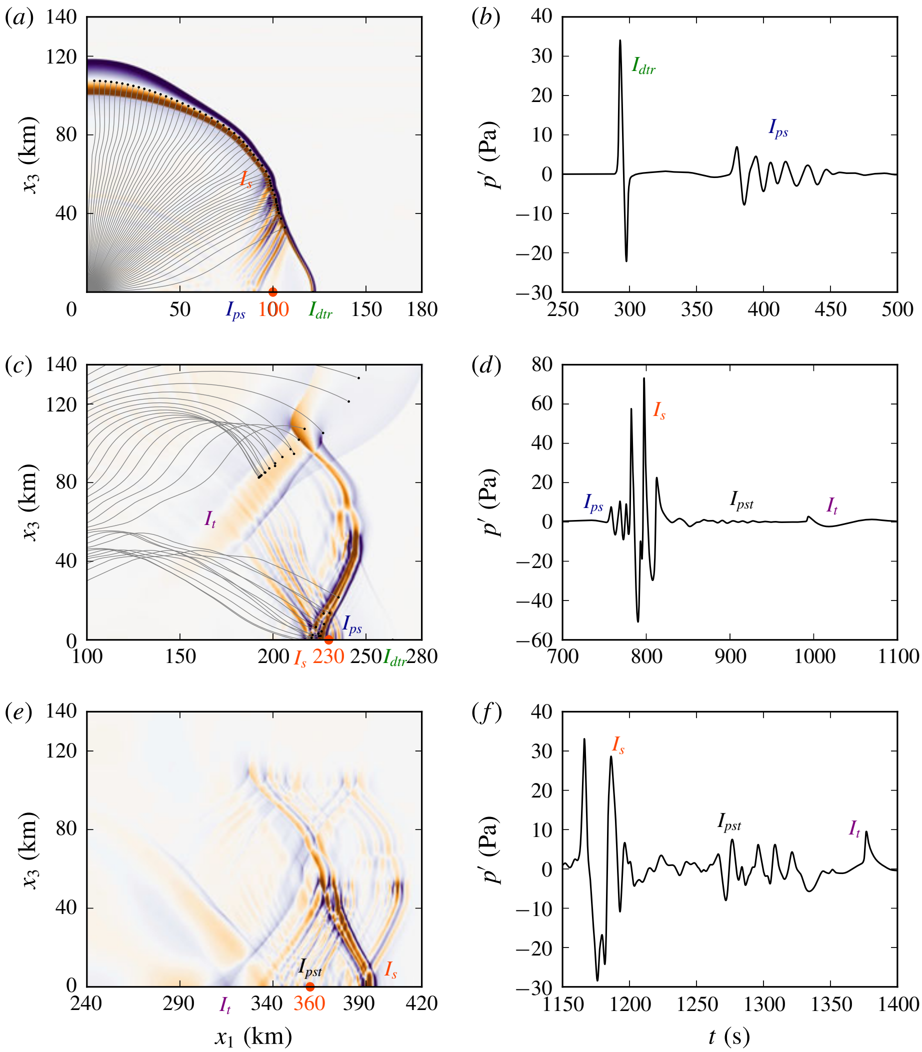

FIGURE 12. (Colour online) Acoustic field Φ on the x_1–x_3 plane at (a) t_3, (c) t_5 and (e) t_7. Pressure signals p' recorded on the x_1 axis at (b) $x_1 = 100$ km, (d) $x_1 = 230$ km and (f) $x_1 = 360$ km. The grey lines in (a,c) represent the acoustic rays.

I_s, becomes visible in figure 12(a) at about 50 km altitude. At the ground station located at $x_1 = 230$ km on the x_1 axis, three different wave packets are recorded along with the partial reflections I_{ps}. The stratospheric phase I_s is observed between 780 and 820 s, with an amplitude equal to about 73 Pa. Furthermore, contrarily to the prediction of ray theory, a thermospheric wave packet I_t is also detected between 980 and 1100 s, with a maximum overpressure of 3 Pa. As discussed in § 4.7, the arrival I_t is due to diffraction at the thermospheric caustic. At $t = t_3$ and $t = t_5$, arch-like structures are observed between the ground and the lower thermosphere. They are associated with partial reflections occurring whenever the wavefront propagates downward or upward through the small-scale inhomogeneous layer. The resulting phase, labelled as I_{pst}, is clearly visible at the ground stations located at $x_1 = 230$ km

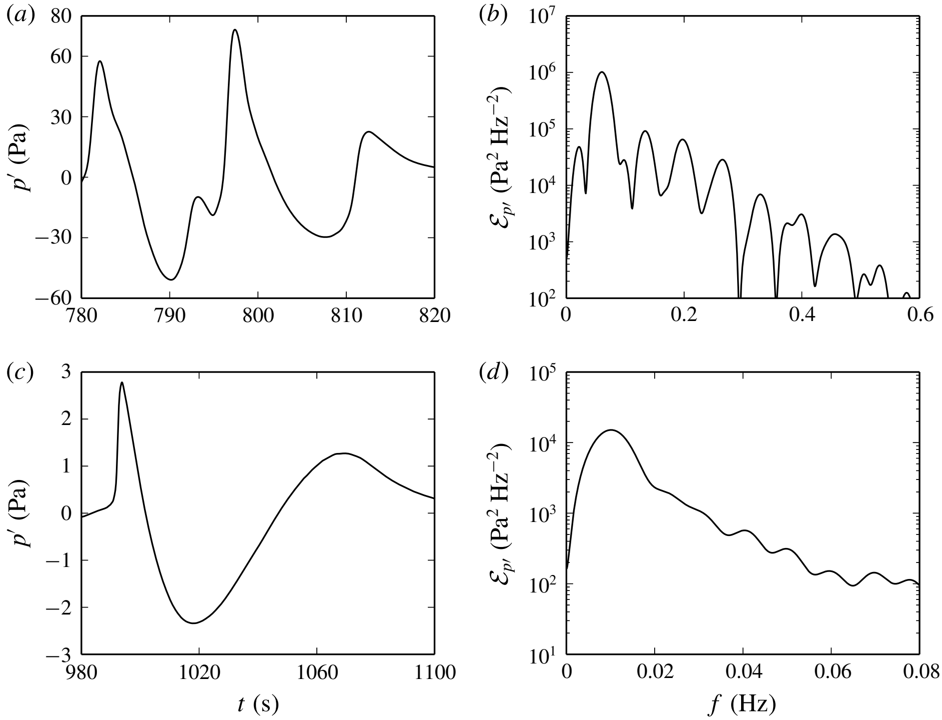

FIGURE 13. Zooms of the pressure signals p' recorded on the x_1 axis at $x_1 = 230$ km. (a) Stratospheric and (c) thermospheric arrivals and (b,d) corresponding spectra.

and at $x_1 = 360$ km. Finally, zooms of the stratospheric and thermospheric arrivals detected at $x_1 = 230$ km are displayed in figures 13(a) and 13(c), respectively. The corresponding energy spectral densities are reported in figures 13(b) and 13(d). Both signals exhibit U-shaped waveforms. Their durations are around 35 and 90 s, and their central frequencies are equal to about 0.06 and 0.01 Hz.

In order to characterize the different arrivals, the pressure perturbation $p'_1(x_1, t) = p'(x_1, 0, 0, t)$ recorded on the x_1 axis is plotted in figure 14(a) as a function of the distance x_1 and of the retarded time $t_r = t - x_1/\bar{c}(0)$. This diagram allows comparison of the arrival times of the various phases with the one of a wave propagating at ground level with a speed equal to $\bar{c}(0)$. Yellow dots are associated with the couples (x_1, t_r) for which an acoustic ray is detected. The maximum in time of the function p'_1 is illustrated in figure 14(b). The direct phase I_{dtr} is recorded without delay, meaning that its propagation speed is close to $\bar{c}(0)$. Its maximum overpressure decreases with range, more rapidly than the amplitude of a spherical wave in a homogeneous medium. As discussed in § 4.5, this decay is associated with the negative gradient of the speed of sound in the troposphere, which deviates the acoustic energy towards the upper atmosphere. The direct phase I_{dtr} represents the dominant contribution up to $x_1 = 130$ km. The partial reflections I_{ps} are detected all along the x_1 axis, with a delay which diminishes with the distance x_1. The amplitude of I_{ps} is of the order of 1 Pa between $x_1 = 0$ km and $x_1 = 70$ km, reaches a local minimum at $x_1 = 70$ km and then increases again up to values of about 15 Pa at $x_1 = 140$ km. In addition, a phase jump of π is observed at $x_1 = 70$ km. The stratospheric arrival I_s is recorded for $x_1 \gtrsim 100$ km, whereas, according to ray theory, it can be detected only for $x_1 \gtrsim 212$ km.

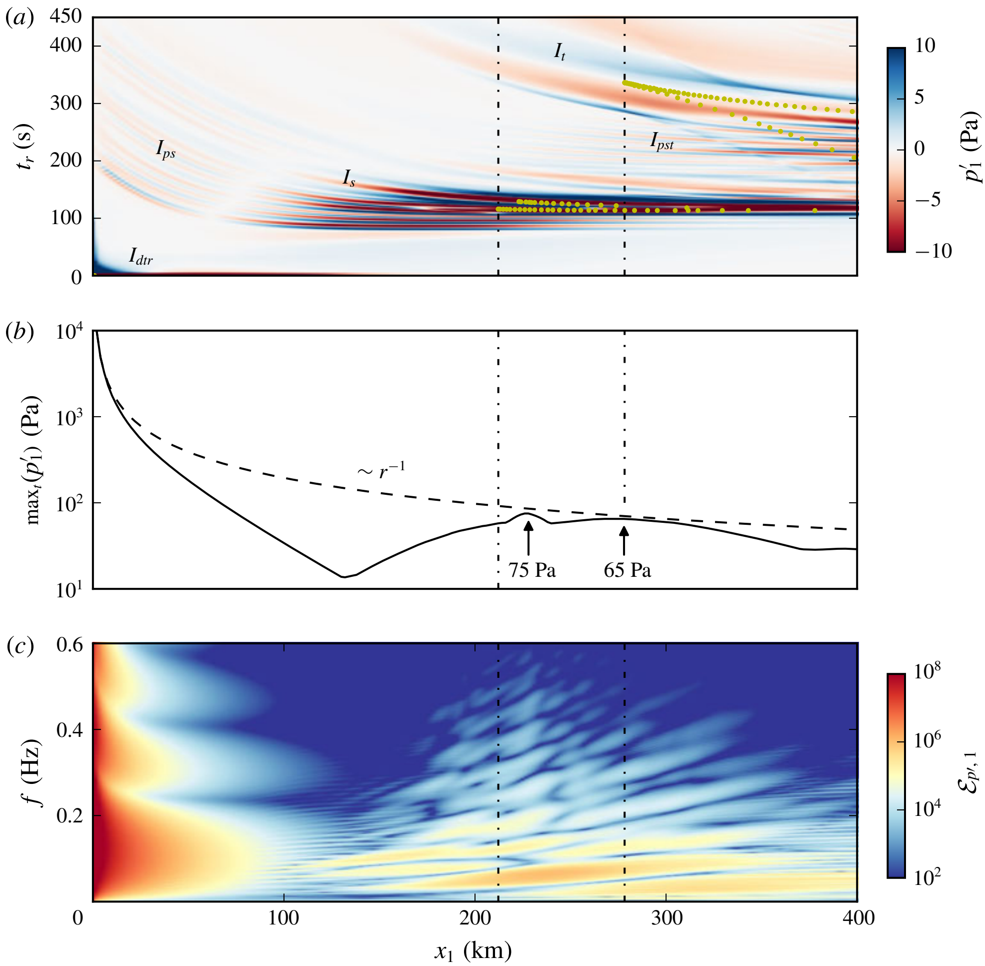

FIGURE 14. (Colour online) (*a*) Pressure p'_1 recorded at ground level as a function of the distance x_1 and of the retarded time t_r. Yellow dots are associated with the couples (x_1, t_r) for which an acoustic ray arrives at the ground. In order to visualize all the infrasonic arrivals, the colour level ranges from −10 to +10 Pa. (*b*) Maximum in time of $p'_1(x_1, t)$ as a function of the distance x_1. The dashed line represents the decay of a spherical wave in a free homogeneous medium. (*c*) Spectrum $\mathcal{E}_{p',1}(x_1, f)$ of the arrivals recorded at ground level as a function of the distance x_1 and of the frequency f.

The stratospheric phase represents the most important contribution to the pressure signal for $x_1 \gtrsim 120$ km. Its amplitude remains higher than 10 Pa up to at least $x_1 = 450$ km, with two local maxima of 75 and 65 Pa at $x_1 = 230$ km and $x_1 = 275$ km, respectively. The thermospheric phase I_t is detected at ground level for $x_1 \gtrsim 180$ km, while the geometrical-acoustics approximation predicts no arrival for $x_1 \lesssim 280$ km. The amplitude of the signal I_t is much lower than the maximum overpressure of the stratospheric wave packet, mainly as a result of the nonlinear lengthening in the upper atmosphere.

The spectrum $\mathcal{E}_{p',1}(x_1, f) = \mathcal{E}_{p'}(x_1, 0, 0, f)$ of the various arrivals recorded at ground level is finally displayed in figure 14(*c*) as a function of the distance along the x_1 axis

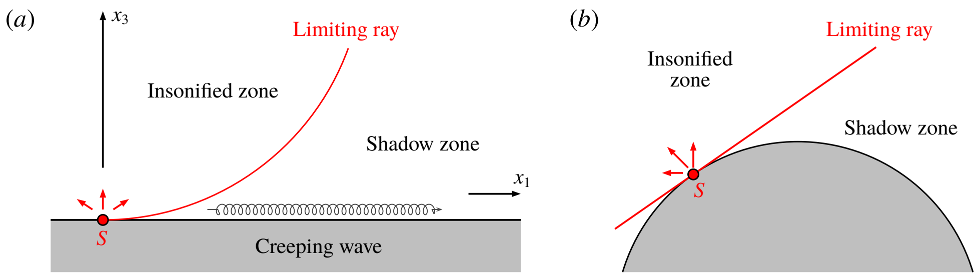

FIGURE 15. (Colour online) Equivalence between (*a*) the sound field above a flat ground in an upward refracting atmosphere and (*b*) the acoustic field above a convex surface in a homogeneous medium.

and of the frequency f. Up to $x_1 = 100$ km, the main contribution is due to the direct phase I_{dtr}, which has an N-waveform, leading to a broadband spectrum $\mathcal{E}_{p',1}$. On the contrary, the energy spectral density $\mathcal{E}_{p',1}$ of the arrivals beyond $x_1 = 100$ km is essentially contained in the frequency range $[0, 0.3]$ Hz.

4.5. *Analysis of the direct arrival* I_{dtr}

As previously mentioned, the direct arrival I_{dtr} is not predicted by the geometrical acoustics. Because of the negative vertical gradient of the speed of sound, rays are deviated towards the upper atmosphere and do not reach the ground up to $x_1 = 212$ km distance from the source location. From a physical point of view, the effect of an inhomogeneous atmosphere can be better understood with the help of an analogy proposed by Pierce (1985) and Berry & Daigle (1988) among others. The sound field above a flat surface in a quiescent and upward refracting atmosphere, i.e. with a negative vertical gradient of the speed of sound, can be considered equivalent to the acoustic field above a curved convex surface in a homogeneous medium, as illustrated in figure 15. In the latter case, the rays emanating from the source are straight lines and, for geometrical reasons, cannot penetrate into the region below the tangent to the curved ground, which is called shadow zone. Hence, in the shadow side of the sound field, no ray can be detected and, according to the geometrical theory, the amplitude of the pressure perturbation p' should be nil. The direct arrival I_{dtr} is thus induced by diffraction and is interpreted as a creeping wave propagating along the x_1 axis.

In order to gain more insight into how acoustic energy penetrates in the shadow zone and, in particular, on the Earth's surface, an analysis of the phase I_{dtr} is carried out in this paragraph. As formerly stated, propagation at ground level is essentially linear, excepting in the source region. Furthermore, viscous and thermal conduction effects play a minor role in the troposphere. Besides, to simplify the forthcoming developments, the mean atmosphere is modelled as an effective quiescent medium with the speed of sound and the density given by $\bar{c}_{eff} = \bar{c} + \bar{u}_1$ and $\bar{\rho}_{eff} = \bar{\rho}\bar{c}^2/\bar{c}_{eff}^2$, respectively. As demonstrated by Godin (2002), such an approximation is valid for low angles of propagation with respect to the horizontal axis, and is consequently justified for a creeping wave. Under the above hypotheses, the acoustic field is axisymmetric and the normalized pressure perturbation $\Phi = p'/\sqrt{\bar{\rho}_{eff}}$ can be described by the wave equation (Bergmann 1946; Pierce 1990)

$$\frac{\partial^2 \Phi}{\partial \varrho^2} + \frac{1}{\varrho}\frac{\partial \Phi}{\partial \varrho} + \frac{\partial^2 \Phi}{\partial x_3^2} + \left[\frac{1}{2\bar{\rho}_{eff}}\frac{\mathrm{d}^2 \bar{\rho}_{eff}}{\mathrm{d}x_3^2} - \frac{3}{4\bar{\rho}_{eff}^2}\left(\frac{\mathrm{d}\bar{\rho}_{eff}}{\mathrm{d}x_3}\right)^2\right]\Phi - \frac{1}{\bar{c}_{eff}^2(x_3)}\frac{\partial^2 \Phi}{\partial t^2} = \frac{G}{\sqrt{\bar{\rho}_{eff}}}, \tag{4.4}$$

where $\varrho = \sqrt{x_1^2 + x_2^2}$ and G is a function of the source terms Λ_ρ and $\Lambda_{\rho e_t}$ in (2.3). Since the characteristic acoustic wavelength $\lambda \simeq 2.6$ km is smaller than the typical length scale for variations of the atmospheric density ($\simeq$8.4 km), the vertical derivatives of the function $\bar{\rho}_{eff}$ are henceforth neglected. Taking the Fourier–Bessel transform

$$\hat{\chi}(k_\varrho, x_3, \omega) = \int_{-\infty}^{+\infty}\int_0^{+\infty} \chi(\varrho, x_3, t)\mathcal{J}_0(k_\varrho \varrho)\mathrm{e}^{+\mathrm{i}\omega t}\varrho\,\mathrm{d}\varrho\,\mathrm{d}t, \tag{4.5}$$

with $\chi = \Phi$ or $\chi = G$ and where $\mathcal{J}_0$ is the zeroth-order Bessel function of the first kind, the depth-separated Helmholtz equation is obtained:

$$\frac{\mathrm{d}^2\hat{\Phi}}{\mathrm{d}x_3^2} + \left(\frac{\omega^2}{\bar{c}_{eff}} - k_\varrho^2\right)\hat{\Phi} = \frac{\hat{G}}{\sqrt{\bar{\rho}_{eff}}}. \tag{4.6}$$

The normalized pressure perturbation Φ is then retrieved by the inverse transform

$$\Phi(\varrho, x_3, t) = \frac{1}{4\pi}\iint_{-\infty}^{+\infty} \Phi(k_\varrho, x_3, \omega)\mathcal{H}_0^{(1)}(k_\varrho \varrho)\mathrm{e}^{-\mathrm{i}\omega t}k_\varrho\,\mathrm{d}k_\varrho\,\mathrm{d}\omega, \tag{4.7}$$

where $\mathcal{H}_0^{(1)}$ is the zeroth-order Hankel function of the first kind. By means of the residue theorem, it is possible to demonstrate that integral (4.7) can be approximated by a linear combination of the eigenfunctions $\hat{\Phi}$ of the differential equation (Jensen *et al.* 2011)

$$\frac{\mathrm{d}^2\hat{\Phi}}{\mathrm{d}x_3^2} + \left(\frac{\omega^2}{\bar{c}_{eff}} - k_\varrho^2\right)\hat{\Phi} = 0, \tag{4.8a}$$

completed with the rigid-wall constraint

$$\frac{\mathrm{d}\hat{\Phi}}{\mathrm{d}x_3} = 0, \quad x_3 = 0 \text{ km}, \tag{4.8b}$$

and with the radiation condition

$$\hat{\Phi} \sim \mathrm{e}^{\mathrm{i}k_3^\infty x_3}, \quad k_3^\infty = \lim_{x_3\to+\infty}\sqrt{\frac{\omega^2}{\bar{c}_{eff}(x_3)} - k_\varrho^2}, \quad x_3 \to +\infty. \tag{4.8c}$$

The real part of the wavenumber k_3^∞ is required to be positive or nil in order for the function $\hat{\Phi}$ to represent an outgoing wave as $x_3 \to +\infty$. Since the diffracted arrival I_{dtr} is mainly influenced by the negative gradient of the temperature in the troposphere, the function $\bar{c}_{eff}$ is here defined as

$$\bar{c}_{eff}(x_3) = \begin{cases} \bar{c}(x_3) + \bar{u}_1(x_3), & x_3 \in [0, x_3^\infty] \\ \bar{c}(x_3^\infty) + \bar{u}_1(x_3^\infty), & x_3 > x_3^\infty, \end{cases} \tag{4.8d}$$

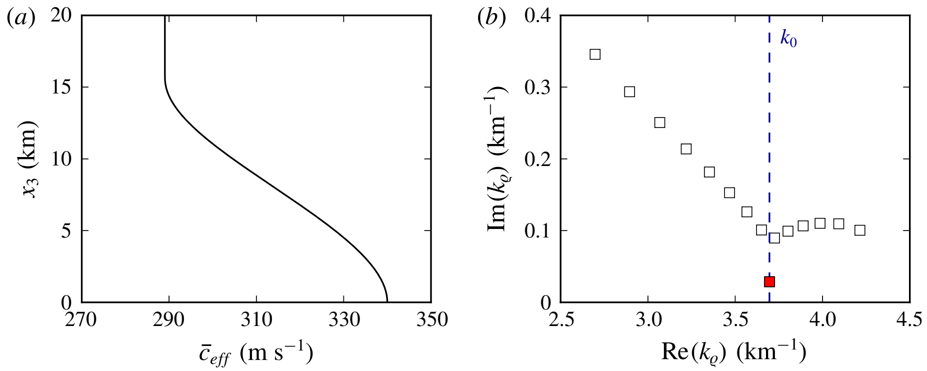

FIGURE 16. (Colour online) (*a*) Effective speed of sound profile $\bar{c}_{eff}$. (*b*) Wavenumbers k_ϱ for $f = 0.2$ Hz; the red square corresponds to the least attenuated mode.

where $x_3^\infty = 15.75$ km is the altitude of the first minimum of the sum $\bar{c}(x_3) + \bar{u}_1(x_3)$. The resulting profile $\bar{c}_{eff}(x_3)$ is displayed in figure 16(*a*). In line with this definition, the above radiation condition is replaced by the following boundary constraint (Jensen *et al.* 2011):

$$\frac{\mathrm{d}\hat{\Phi}}{\mathrm{d}x_3} - \mathrm{i}k_3^\infty \hat{\Phi} = 0, \quad k_3^\infty = \sqrt{\frac{\omega^2}{\bar{c}_{eff}(x_3^\infty)} - k_\varrho^2}, \quad x_3 = x_3^\infty. \tag{4.8e}$$

Problem (4.8) represents a differential eigensystem and can be solved through a pseudospectral collocation method (Bertin *et al.* 2014; Sabatini & Bailly 2015). As an illustration, the eigenvalues k_ϱ obtained for $f = 0.2$ Hz are plotted in figure 16(*b*). As suggested by Pierce (1985), along the x_1 axis, integral (4.7) is dominated by wavenumbers k_ϱ close to $k_0 = \omega/\bar{c}_{eff}(0)$. Moreover, since the imaginary parts of the eigenvalues k_ϱ are strictly positive, the corresponding contributions, which are proportional to $\mathcal{H}_0^{(1)}(k_\varrho r)$, decay with distance. Consequently, at large distances, only the least attenuated mode is likely to be observed. The phase speed $v_\phi = \omega/\mathrm{Re}(k_\varrho)$ and the imaginary part $\alpha = \min_{k_\varrho}(\mathrm{Im}(k_\varrho))$ of the least attenuated mode are depicted as functions of the frequency f in figure 17(*a*). Globally, they both depend weakly on the pulsation ω. For $f > 0.05$ Hz, the velocity v_ϕ is approximately equal to $\bar{c}_{eff}(0) = 340$ m s^{-1}, and the attenuation factor α increases only slightly as f augments and has an average value of about $\alpha_{mean} = 2.85 \times 10^{-2}$ km^{-1} in the range $[0.05, 0.2]$ Hz. As the wind velocity is nil at ground level, the least attenuated mode propagates with a celerity equal to the speed of sound on the Earth's surface, $\bar{c}(0)$, which confirms the result of the previous paragraph. Moreover, by virtue of the above considerations, the absolute value of the pressure perturbation p' along the x_1 axis and in the far range is found to behave as

$$p'(x_1, 0, 0, t) \propto \frac{1}{\sqrt{x_1}} \mathrm{e}^{-\alpha_{mean} x_1}, \tag{4.9}$$

since $\mathcal{H}_0^{(1)}(k_\varrho x_1) \sim 1/\sqrt{x_1}$ for $k_\varrho x_1 \gg 1$. Hence, conforming to earlier remarks, the amplitude of the phase I_{dtr} weakens more rapidly than that of a spherical wave in a homogeneous medium, for which $p'(x_1, 0, 0, t) \propto 1/x_1$. To conclude, the maximum in

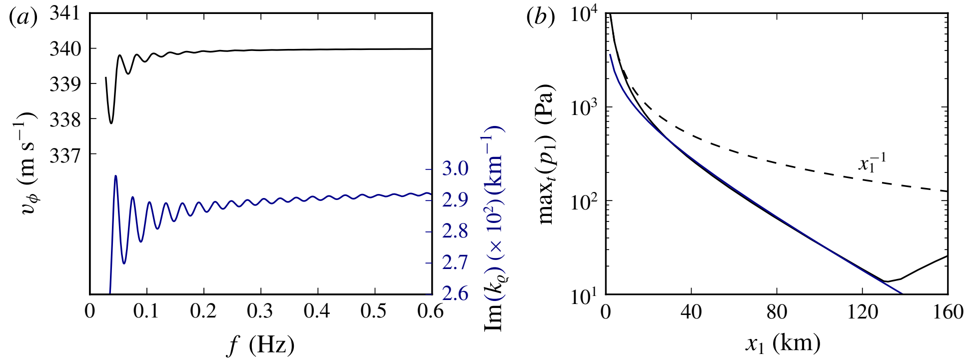

FIGURE 17. (Colour online) (*a*) Phase speed (black line) and imaginary part (blue line) of the least attenuated mode. (*b*) Maximum in time of the function $p_1'(x_1, t)$ as a function of the distance x_1, compared to the result given by formula (4.9) and to the behaviour of a spherical wave in a homogeneous medium.

time of the function p_1' is again illustrated in figure 17(*b*) and compared to the result given by expression (4.9). A very good agreement is observed between numerical and theoretical predictions for $x_1 > 20$ km.

4.6. *Analysis of the partial reflections*

The sensitivity of ground recordings to the speed of sound and wind fluctuations of length scale of the same order as the acoustic wavelength has received particular attention in recent years (Chunchuzov *et al.* 2011, 2014, 2015; Bertin *et al.* 2014). In particular, Chunchuzov *et al.* (2014, 2015) demonstrated the feasibility of retrieving the vertical structure of the atmosphere from the reflected signals, whose energy spectral densities are closely related to the characteristic wavenumbers of the inhomogeneities. In order to gain more insight into the relationship between the wavenumber spectrum of the atmospheric fluctuations and the Fourier transform of the partial reflections, a more detailed analysis of the phase I_{ps} is now carried out on a simplified model.

4.6.1. *Reflection of a spherical wave by a one-dimensional speed-of-sound inhomogeneity*

The configuration schematically illustrated in figure 18 is considered. A spherical wavefront is emitted in an infinite domain $Ox_1x_2x_3$ by a point source placed at the origin O and propagates through a one-dimensional speed-of-sound inhomogeneity confined between the altitudes x_{3wb} and x_{3wt}; the medium is at rest and the speed of sound away from the inhomogeneity is equal to $\bar{c}_\infty$. The interaction between the wavefront and the speed-of-sound fluctuation generates a transmitted wave and a reflected wave. In order to simplify the analytical developments, nonlinear, viscous and thermal conduction effects are henceforth neglected. Moreover, since the large-scale variations of the atmospheric medium induced by the gravitational acceleration do not contribute to the reflected wave, the gradient $\mathrm{d}\bar{p}/\mathrm{d}x_3$ is assumed nil and the ambient pressure $\bar{p}$ is set equal to $\bar{p}_0$. Under these hypotheses, the pressure perturbation p' is described by the wave equation (Bergmann 1946; Pierce 1990)

$$\frac{\partial^2 p'}{\partial x_1^2} + \frac{\partial^2 p'}{\partial x_2^2} + \bar{\rho}(x_3)\frac{\partial}{\partial x_3}\left(\frac{1}{\rho(x_3)}\frac{\partial p'}{\partial x_3}\right) - \frac{1}{\bar{c}^2(x_3)}\frac{\partial^2 p'}{\partial t^2} = -F(t)\delta(\boldsymbol{x}), \tag{4.10}$$

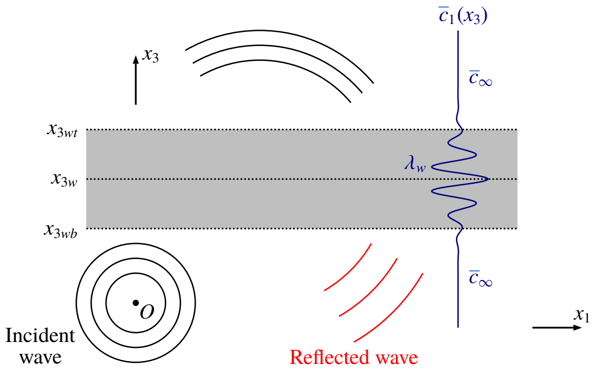

FIGURE 18. (Colour online) Propagation of a spherical wave through a small-scale speed-of-sound inhomogeneity.

where $F(t)$ indicates the temporal envelope of the point source and $\bar{\rho}(x_3) = \gamma \bar{p}_0/\bar{c}^2(x_3)$. As shown in appendix B, for $x_3 \ll x_{3w}$, the incident sound field $p_i'(\boldsymbol{x}, t)$ is represented by

$$p_i'(\boldsymbol{x}, t) = \frac{F(t - \|\boldsymbol{x}\|/\bar{c}_\infty)}{4\pi\|\boldsymbol{x}\|}. \tag{4.11}$$

Accordingly, the temporal shape of the source is advected in space at the speed $\bar{c}_\infty$ and the maximum overpressure decays as $1/\|\boldsymbol{x}\|$. Moreover, the temporal Fourier transform $\hat{p}_r'(\boldsymbol{x}, \omega)$ of the reflected wave $p_r'(\boldsymbol{x}, t)$,

$$\hat{p}_r'(\boldsymbol{x}, \omega) = \int_{-\infty}^{+\infty} p_r'(\boldsymbol{x}, t) \mathrm{e}^{\mathrm{i}\omega t}\, \mathrm{d}t, \tag{4.12}$$

is given by the integral

$$\hat{p}_r'(\boldsymbol{x}, \omega) = \frac{\hat{F}(\omega)}{4\pi} \iint_{-\infty}^{+\infty} \frac{\mathrm{i}\mathcal{R}_c \mathrm{e}^{+\mathrm{i}[k_1x_1 + k_2x_2 - k_3(k_1,k_2,\omega)x_3]}}{2\pi k_3(k_1, k_2, \omega)}\, \mathrm{d}k_1\, \mathrm{d}k_2, \tag{4.13}$$

where k_1, k_2 and $k_3 = \sqrt{(\omega/\bar{c}_\infty)^2 - (k_1^2 + k_2^2)}$ represent the wavenumber components, $\hat{F}$ is the Fourier transform of $F(t)$ and $\mathcal{R}_c$ is the reflection coefficient of the inhomogeneous layer. The acoustic field $\hat{p}_r'$ can be interpreted as a sum of monochromatic plane waves whose amplitude is proportional to both the incident spectrum $\hat{F}$ and the reflection coefficient $\mathcal{R}_c$. The value of $\mathcal{R}_c$ depends on the speed of sound $\bar{c}(x_3)$, on the incidence angle $\varphi = \mathrm{atan}(k_3/\sqrt{k_1^2 + k_2^2})$ with respect to the horizontal plane and on the pulsation ω. According to Lekner (1987), the reflection coefficient $\mathcal{R}_c$ is defined as the limit

$$\mathcal{R}_c \equiv \lim_{x_3 \to -\infty} r_c(x_3) \mathrm{e}^{2\mathrm{i}\tilde{k}_3(x_3)x_3}, \tag{4.14}$$

where the wavenumber $\tilde{k}_3$ is given by

$$\tilde{k}_3^2(x_3) \equiv \frac{\omega^2}{\bar{c}^2(x_3)} - k_1^2 - k_2^2 = \frac{\omega^2}{\bar{c}^2(x_3)} - \frac{\omega^2}{\bar{c}_\infty^2} \cos^2(\varphi), \tag{4.15}$$

and the function $r_c(x_3)$ satisfies the Riccati problem

$$\frac{\mathrm{d}r_c}{\mathrm{d}x_3} + 2\mathrm{i}\tilde{k}_3 r_c - \frac{\bar{\rho}}{2\tilde{k}_3}\frac{\mathrm{d}(\tilde{k}_3/\bar{\rho})}{\mathrm{d}x_3}(1 - r_c^2) = 0, \tag{4.16}$$

with the condition

$$\lim_{x_3 \to +\infty} r_c = 0. \tag{4.17}$$

Since the inhomogeneous layer is assumed confined in the interval $[x_{3wb}, x_{3wt}]$, $r_c(x_3^{\infty}) = 0$ for $x_3^{\infty} > x_{3wt}$ and the above equation can be integrated from $x_3 = x_3^{\infty}$ to $x_3 = x_3^{-\infty} < x_{3wb}$ through any stable time-integration algorithm.

4.6.2. *Reflection coefficient of a Morlet wavelet*

The reflection coefficient is now analysed for a speed of sound $\bar{c}(x_3)$ defined as the sum of a constant $\bar{c}_{\infty}$ and an elementary Morlet wavelet of amplitude $\epsilon_{\bar{c}}\bar{c}_{\infty}$, of wavelength λ_w and located at altitude x_{3w}:

$$\bar{c}(x_3) = \bar{c}_{\infty}[1 + \epsilon_{\bar{c}}\mathrm{e}^{-z^2/2}\cos(2\pi z)], \quad \text{with } z = \frac{x_3 - x_{3w}}{\lambda_w}. \tag{4.18}$$

Hereafter, the parameter $\epsilon_{\bar{c}}$ will be considered small. The modulus $|\mathcal{R}_c|$ obtained with $\epsilon_{\bar{c}}\bar{c}_{\infty} = 5\ \mathrm{m\ s^{-1}}$ is plotted in figure 19 as a function of the normalized pulsation $\omega\lambda_w/\bar{c}_{\infty}$ and of the sinus of the incidence angle φ. The function $|\mathcal{R}_c|$ is different from zero only in specific frequency bands and its maxima approximately satisfy the well-known Bragg law (Blanc-Benon, Dallois & Juvé 2001)

$$2\lambda_w \sin(\varphi) = l\lambda, \tag{4.19}$$

where l is an integer number and $\lambda = 2\pi\bar{c}_{\infty}/\omega$ is the incident wavelength. The modulus $|\mathcal{R}_c|$ increases as φ tends to 0, and is close to 1 for incidences φ lower than about 10°. In this case, the associated plane wave is totally reflected. Moreover, in each frequency band, there exists an angle φ_t, called intromission angle, for which $\mathcal{R}_c$ is nil and the signal is totally transmitted. As an example, φ_t is equal to 45° for $l = 1$ and to about 57.3° for $l = 2$.

According to Lekner (1987), under the hypothesis of weak reflection, a first approximation of the function $\mathcal{R}_c$ for a generic inhomogeneity $\bar{c}' = \bar{c} - \bar{c}_{\infty}$ is given by the integral

$$\mathcal{R}_c \simeq \int_{-\infty}^{+\infty} \left[\frac{\mathrm{i}\Delta\tilde{k}_3^2}{2k_3} + \frac{1}{2}\frac{1}{\bar{\rho}}\frac{\mathrm{d}\bar{\rho}}{\mathrm{d}x_3}\right] \mathrm{e}^{2\mathrm{i}k_3x_3}\,\mathrm{d}x_3, \quad \text{with } \Delta\tilde{k}_3^2(x_3) = \frac{\omega^2}{\bar{c}^2(x_3)} - \frac{\omega^2}{\bar{c}_{\infty}^2}. \tag{4.20}$$

For weak inhomogeneities ($\bar{c}'/\bar{c}_{\infty} \ll 1$), the density gradient can be rewritten as $(\mathrm{d}\bar{\rho}/\mathrm{d}x_3)/\bar{\rho} = -2(\mathrm{d}\bar{c}'/\mathrm{d}x_3)/\bar{c}_{\infty}$. As a result, integral (4.20) can be further simplified as

$$\mathcal{R}_c \simeq \mathrm{i}\frac{1}{k_3}\frac{\omega^2}{\bar{c}_{\infty}^2}(2\sin^2(\varphi) - 1)\int_{-\infty}^{+\infty} \frac{\bar{c}'(x_3)}{\bar{c}_{\infty}}\mathrm{e}^{2\mathrm{i}k_3x_3}\,\mathrm{d}x_3. \tag{4.21}$$

This formula allows relating the reflection coefficient $\mathcal{R}_c$ to the spectrum of the speed of sound fluctuations; $\mathcal{R}_c$ is indeed proportional to the Fourier transform of the inhomogeneity $\bar{c}'/\bar{c}_{\infty}$. Furthermore, because of the factor $(2\sin^2(\varphi) - 1)$, the function $\mathcal{R}_c$ vanishes for $\varphi = \varphi_t = 45°$. Hence, the existence of an intromission angle φ_t is not

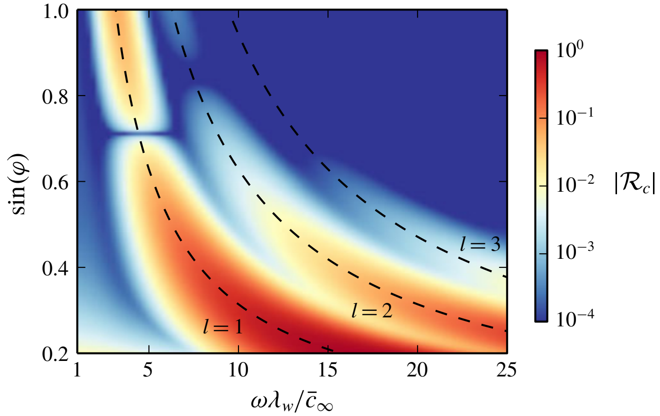

FIGURE 19. (Colour online) Reflection coefficient $\mathcal{R}_c$ for the speed of sound profile (4.18) as a function of the normalized pulsation $\omega\lambda_w\bar{c}_\infty$ and of the sinus of the incidence angle $\sin(\varphi)$. The dashed lines represent the well-known Bragg law $2\lambda_w \sin(\varphi)=l\lambda$, for $l=1$, $l=2$ and $l=3$.

peculiar to the profile (4.18) and is strictly linked to the density variations $(\mathrm{d}\bar{\rho}/\mathrm{d}x_3)/\bar{\rho}$, which, under the assumption $\mathrm{d}\bar{p}/\mathrm{d}x_3=0$, are only induced by the gradient of the speed of sound $\mathrm{d}\bar{c}'/\mathrm{d}x_3$. For $\varphi=\varphi_t$, the effect of the fluctuations of $\bar{\rho}$ is exactly compensated by the effect of the speed-of-sound inhomogeneity.

To conclude, for the specific case of the profile (4.18), it can be shown that the reflection coefficient $\mathcal{R}_c$ can be written as $\mathcal{R}_c \equiv \mathcal{R}\mathrm{e}^{2\mathrm{i}k_3\lambda_w}$, where the auxiliary function $\mathcal{R}$ is approximately equal to

$$\mathcal{R} \simeq \mathrm{i}\frac{\sqrt{2\pi}\,\epsilon_{\bar{c}}}{k_3\lambda_w}\frac{\omega^2\lambda_w^2}{\bar{c}_\infty^2}(2\sin^2(\varphi)-1)\mathrm{e}^{-2k_3^2\lambda_w^2-2\pi^2}\cosh(4\pi k_3\lambda_w). \tag{4.22}$$

This function takes pure imaginary values and exhibits a jump of π at the intromission angle $\varphi=\varphi_t$. Moreover, the modulus $|\mathcal{R}_c|=|\mathcal{R}|$ increases linearly with the amplitude of the speed-of-sound inhomogeneity.

4.6.3. *Amplitude of the wave reflected by a Morlet wavelet along the x_1 axis*

By using the auxiliary variable $\mathcal{R}$, the reflected sound field (4.13) can be recast as follows:

$$\hat{p}_r'(\boldsymbol{x},\omega)=\frac{\hat{F}(\omega)}{4\pi}\iint_{-\infty}^{+\infty}\frac{\mathrm{i}\mathcal{R}\mathrm{e}^{+\mathrm{i}[k_1x_1+k_2x_2-k_3(k_1,k_2,\omega)(x_3-2x_{3w})]}}{2\pi k_3(k_1,k_2,\omega)}\,\mathrm{d}k_1\,\mathrm{d}k_2. \tag{4.23}$$

This integral can be drastically simplified through the method of the stationary phase (Frisk 1994). More specifically, with reference to figure 20, it can be shown that, at a given recording station S_R, the function $\hat{p}_r'(\boldsymbol{x},\omega)$ can be approximated as

$$\hat{p}_r'(\boldsymbol{x},\omega)\simeq\hat{F}(\omega)\mathcal{R}(\varphi_{st},\omega)\frac{\mathrm{e}^{-\mathrm{i}\omega r_\star/\bar{c}_\infty}}{4\pi r_\star}, \tag{4.24}$$

where $\varphi_{st}=\mathrm{atan}(x_{3w}/(\sqrt{x_1^2+x_2^2}/2))$ and $r_\star=\|\overrightarrow{O'S_R}\|$. The variable φ_{st} represents the angle formed with the horizontal plane by the line connecting the source O

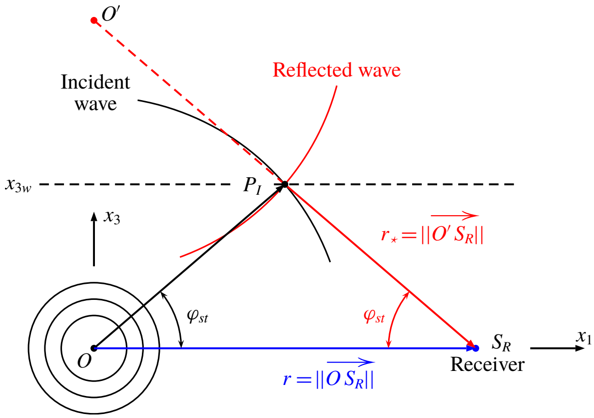

FIGURE 20. (Colour online) Propagation of a spherical wave through a small-scale inhomogeneity. At the receiver S_R, the main contribution to the reflected wave comes from the specular angle φ_{st}, formed with the x_1 axis by the ray connecting the point source O and the intersection between the incident spherical wave and the symmetry axis of the inhomogeneity.

with the intersection point between the incident wavefront and the symmetry axis $x_3 = x_{3w}$ of the speed-of-sound profile; the term $r_\star$ is the distance between the point O', located at the altitude $x_3 = 2x_{3w}$, and the recording station S_R. From a physical point of view, equation (4.24) states that the reflected field $\hat{p}'_r$ consists of a spherical wave emanating from the image source O', whose amplitude is proportional to the incident spectrum $\hat{F}(\omega)$ and to the reflection coefficient $\mathcal{R}$ for a plane wave having an incidence angle equal to the specular angle $\varphi = \varphi_{st}$. Expression (4.24) represents the geometrical approximation of the reflected field, according to which the reflected energy is mainly concentrated in the direction of the specular angle. The modulus $|\hat{p}'_r|$ is finally given by the relation

$$|\hat{p}'_r(\boldsymbol{x}, \omega)| \simeq \left| \frac{\hat{F}(\omega)\mathcal{R}(\varphi_{st}, \omega)}{4\pi r_\star} \right|. \tag{4.25}$$

Since the reflection coefficient $|\mathcal{R}|$ is different from zero only in particular frequency bands, the above formula states that the inhomogeneous layer acts as a selective filter which reflects only specific wavelengths of the incident spectrum.

4.6.4. *Reflection coefficient of a wind inhomogeneity*

The above results, obtained for a small-scale speed-of-sound inhomogeneity, cannot be readily extended to the case of wind fluctuations. However, two-dimensional simulations carried out by the authors suggest that, for incidences φ lower than the intromission angle φ_t and within the limits of validity of the effective celerity approximation (Godin 2002), the effect of a wind inhomogeneity equal to $\bar{u}_1 = \bar{c}'$ in an isothermal atmosphere is closely equivalent to that of the speed-of-sound fluctuation $\bar{c}'$ in a medium at rest. On the contrary, for incidences φ higher than the intromission angle φ_t, a horizontal wind does not contribute to the reflected field.

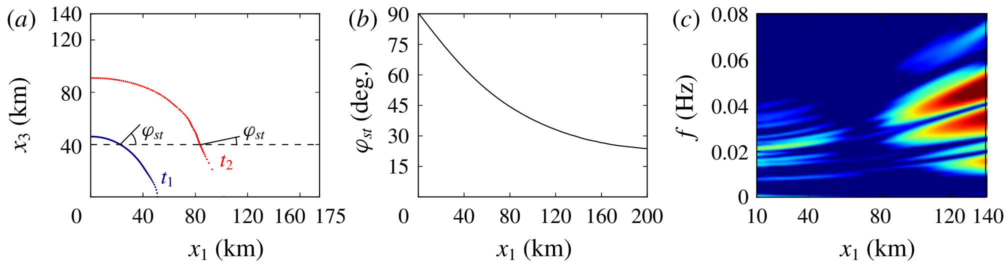

FIGURE 21. (Colour online) (*a*) Wavefronts obtained by ray theory at two different instants of time. (*b*) Angle φ_{st} between the geometrical wavefront and the reference axis $x_3 = 40$ km as a function of the distance x_1 of the receiver. (*c*) Spectrum of the arrival I_{ps} as a function of the distance x_1 and of the frequency f.

4.6.5. *Nonlinear effects on the partial reflections*

As a result of the nonlinear steepening and lengthening, the spectrum of the incident wave p'_i evolves while the wavefront travels from the source location to the small-scale inhomogeneity. Oppositely, the reflected wave p'_r has generally a small amplitude, so that its propagation towards the Earth's surface can be considered linear. Accordingly, supposing that the Fourier transform of the incident signal does not change significantly as this latter crosses the small-scale fluctuation, formula (4.25) remains valid as long as the function $\hat{F}(\omega)$ is interpreted as the incident spectrum at the inhomogeneity location.

4.6.6. *Qualitative analysis of the spectrum of the phase I_{ps}*

The considerations developed in the present section ultimately allow one to qualitatively explain the behaviour of the spectrum of the arrival I_{ps}. It is first remembered that the speed-of-sound and wind fluctuations contributing to the partial reflections are essentially localized between 25 and 55 km altitude, so that their reference axis x_{3w} can be placed at approximately 40 km altitude. Moreover, as shown in figure 21(*a*,*b*), the angle φ_{st} between the wavefront and the layer diminishes with x_1, $\varphi_{st} = 90°$ for $x_1 = 0$ km and tends to 0° with growing values of x_1. Therefore, the evolution with x_1 of the spectrum of the phase I_{ps} can be directly deduced by the behaviour of the reflection coefficient $\mathcal{R}$ as the sinus of the angle φ_{st} goes from 1 to 0. The energy spectral density $\mathcal{E}_{p',1}(x_1, f)$ of the arrivals I_{ps} recorded on the x_1 axis is illustrated in figure 21(*c*) as a function of the distance x_1 and of the frequency f. The maximum of overpressure detected up to $x_1 = 70$ km is around 1 Pa. The minimum of amplitude at about 70 km distance can be justified by considering that, for $x_1 = 70$ km, the angle φ_{st} is close to the intromission angle $\varphi_t = 45°$ (see figure 21*b*). Finally, for $x_1 > 70$ km, the amplitude of the arrival I_{ps} increases because of the diminution of the incidence angle φ_{st} and the subsequent augmentation of the reflection coefficient. As an example, the maximum of overpressure at $x_1 = 140$ km from the source position is around 15 Pa. Besides, as predicted by the Bragg law, the main frequency of the partial reflections I_{ps} globally grows as the distance x_1 increases and the term $\sin(\varphi)$ diminishes. To conclude, the spectrum $\mathcal{E}_{p',1}$ remarkably widens beyond the ground station located at $x_1 = 70$ km distance. This enlargement can be attributed to the fact that the speed-of-sound and wind fluctuations tend to be less selective as the function $\sin(\varphi)$ goes to 0.

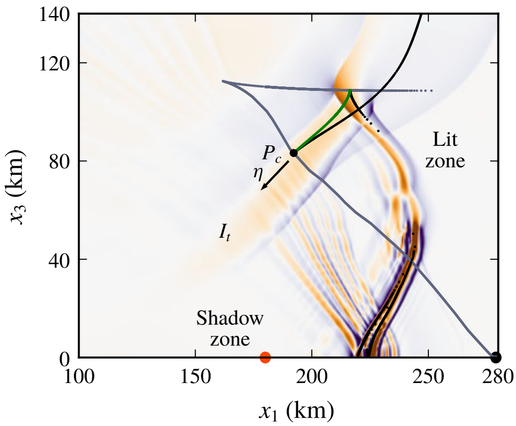

FIGURE 22. (Colour online) Normalized pressure field Φ obtained on the x_1–x_3 plane at $t = 775.89$ s. The grey line represents the thermospheric caustic, whereas the green and black lines constitute the wavefront obtained by ray theory.

4.7. *Diffraction at the thermospheric caustic*

As previously mentioned, diffraction at caustics plays a significant role in atmospheric infrasound propagation. In order to demonstrate the importance of this phenomenon, a more detailed study of the thermospheric caustic is finally carried out.

A caustic is defined within the framework of geometrical acoustics and corresponds to the locus of points where the ray-tube area vanishes, or, equivalently, to the locus of points where two infinitely adjacent rays intersect. The projection on the x_1–x_3 plane of the thermospheric caustic associated with the profiles of the speed of sound and the wind employed in the present simulation is plotted in grey in figure 22. The normalized pressure field Φ obtained at t_5 is displayed as well, along with the wavefront computed by ray theory, which is represented by the green and black curves. The caustic divides the acoustic field into two regions, an ensonified zone between the grey lines, also called a lit region, and a shadow zone. In the context of the geometrical-acoustics approximation, the amplitude of the pressure field should be different from zero only in the lit region. However, as shown in figure 22, part of the acoustic energy penetrates in the shadow zone by diffraction. For this reason, the thermospheric signal I_t is first recorded at about $x_1 = 180$ km on the Earth's surface (red point in figure 22), whereas, according to ray theory, no thermospheric arrival should be detected between the source location and $x_1 = 280$ km (black point in figure 22) corresponding to the intersection between the caustic and the axis x_1.

The energy spectral density $\mathcal{E}_{\Phi,\eta}$ of the signals recorded along the axis η, perpendicular to the caustic at the point P_c (cf. figure 22), is illustrated in figure 23(*a*) as a function of the distance η and of the frequency f. The spectrum of the diffracted field is mainly concentrated around $f = 0.01$ Hz. Its behaviour along the axis η for $f = 0.01$ Hz is plotted in figure 23(*b*). In the shadow zone, for $\eta > 0$ (at the right of the red dashed line), the energy spectral density $\mathcal{E}_{\Phi,\eta}$ exhibits an exponential-like decay. This result can be qualitatively explained by the linear theory of diffraction, according to which the amplitude of a spectral component of the pressure field, having frequency equal to f, decreases as $\mathrm{Ai}(\tilde{\eta}) \sim \tilde{\eta}^{-1/4}\mathrm{e}^{-2/3\tilde{\eta}^{3/2}}$, where Ai is the Airy function of the first kind and $\tilde{\eta}$ is a non-dimensional variable proportional to $\eta f^{2/3}$.

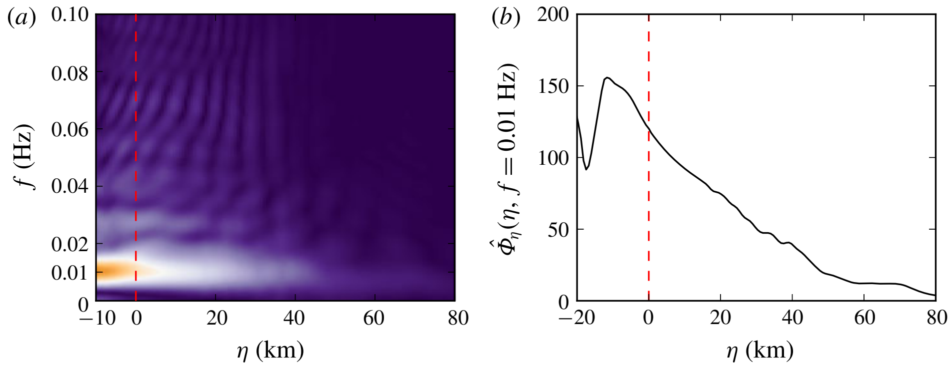

FIGURE 23. (Colour online) (*a*) Energy spectral density $\mathcal{E}_{\Phi,\eta}(\eta, f)$ of the signals recorded along the axis η, normal to the caustic at the point $P_c = (192.2\ \text{km}, 0\ \text{km}, 83.25\ \text{km})$. (*b*) Energy spectral density $\mathcal{E}_{\Phi,\eta}(\eta, f)$ for $f = 0.01$ Hz.

The dependence of $\tilde{\eta}$ on the frequency f also allows one to argue that the distance x_1 on the ground at which the thermospheric arrival I_t is first detected augments with the amplitude of the source. Indeed, as the source energy increases, the lengthening of the N-wave is enhanced by the nonlinear effects in the upper atmosphere. As a result, the central frequency of the signal reaching the caustic decreases, the decay of the Airy function slows down and the penetration depth in the shadow zone grows.

To conclude, the wavefront obtained by ray theory is also represented in figure 22 by the green and black lines. Within the framework of geometrical acoustics, it can be shown that the waveform on the green side of the wavefront is given by the Hilbert transform of the waveform on the black side, at least in the linear regime (Pierce 1985). This result allows one to qualitatively understand the origin of the U-shaped signature of the thermospheric arrival (see figure 13*c*), which corresponds to the Hilbert transform of the N-shaped waveform generated by the impulsive source.

5. Concluding remarks

A direct computation of the propagation of an infrasonic impulse signal in a stratified atmospheric mean flow is performed in this study. To this end, high-fidelity numerical schemes, previously developed for applications in computational aeroacoustics, are employed. To the best of the authors' knowledge, this is the first time the Navier–Stokes equations have been applied to the analysis of the three-dimensional propagation of low-frequency signals in the atmosphere. All the main phenomena affecting infrasonic waves, including convection, refraction, diffraction, absorption as well as nonlinear effects, are accurately reproduced, allowing a fine physical analysis of the various arrivals observed at ground level.

The waveform of the thermospheric phase is found to be significantly altered in the upper atmosphere. Contrarily to the predictions of the weakly nonlinear ray theory, the strong nonlinear effects mainly induced by the stratification may lead to a non-self-similar distortion of an N-wave propagating upwards. The continuous partial reflections generated as the wavefront travels through the small-scale speed-of-sound and wind fluctuations located in the stratosphere are analysed as well. The inhomogeneous layer acts as a selective filter, which reflects only specific wavelengths of the incident wave. An analytical model of the transfer function of such a filter, based on a simplified representation of the stratified mean flow, is proposed to interpret the evolution with the distance from the source of the spectrum of the partial reflections recorded on the Earth's surface. Finally, as a consequence of the diffraction at the thermospheric caustic, the acoustic levels in the shadow zone are shown to be affected by the amplitude of the impulsive source.

All the present findings could not be obtained through the methods classically employed for the study of acoustic waves, which demonstrates the attractiveness of investigations based on the full Navier–Stokes equations. A general and complete picture of infrasound propagation is here offered, for the first time in three dimensions. A quantitative comparison between numerical results and ground-recorded signals is however still difficult to carry out for various reasons. On the one hand, a direct numerical simulation of the governing equations may be computationally unaffordable for sources of higher frequency. On the other hand, the sensitivity of the ground recordings to the small-scale fluctuations of the profiles of the speed of sound and the wind evidences the need for a fine description of the three-dimensional turbulent atmospheric mean flow. These two topics will be the subject of future research work.

Acknowledgements

The presented results have been obtained within the framework of LETMA (Laboratoire ÉTudes et Modélisation Acoustique), a Contractual Research Laboratory shared between CEA, CNRS, École Centrale de Lyon, C-Innov and Université Pierre et Marie Curie. This work was granted access to the HPC resources of the Très Grand Centre de calcul du CEA (TGCC) under the allocation 2015-200204 made by GENCI (Grand Equipement National de Calcul Intensif). The authors express gratitude to the Direction Générale de l'Armement (DGA) for financial support. The authors would also like to thank Ludovic Aubry for his precious help in debugging the solver, Dr N. Lardjane and Dr J. Snively for stimulating discussions.

Appendix A. Source forcing terms

In the present study, the infrasonic source is modelled by the terms Λ_ρ and $\Lambda_{\rho e_t}$ on the right-hand sides of the continuity and energy conservation equations. It is well known that the perturbations of density and pressure of an acoustic wave are approximately linked by the isentropic relation $p' = \bar{c}^2\rho'$ (Whitham 1974). Therefore, in order to mainly excite the acoustic modes of the atmosphere and to limit the energy delivered to gravity modes, the function Λ_ρ is defined as

$$\Lambda_\rho(\boldsymbol{x}, t) = \frac{\gamma - 1}{\bar{c}^2(x_3)}\Lambda_{\rho e_t}(\boldsymbol{x}, t). \tag{A 1}$$

The term $\Lambda_{\rho e_t}$ is then designed to obtain a blast wave, which is typical of explosions Whitham (1974). In order to justify the choice of the temporal envelope of the function $\Lambda_{\rho e_t}(\boldsymbol{x}, t)$, it is worth considering the simplified case of the isentropic propagation in a homogeneous medium, when nonlinear, viscous and thermal conduction effects are neglected. Under these hypotheses, it is straightforward to show that the Navier–Stokes equations (2.3) reduce to

$$\frac{\partial^2 p'}{\partial t^2} - \bar{c}^2\frac{\partial^2 p'}{\partial x_i \partial x_i} = (\gamma - 1)\frac{\partial \Lambda_{\rho e_t}}{\partial t}. \tag{A 2}$$

As a consequence, the waveform is mainly driven by the temporal derivative $\partial\Lambda_{\rho e_t}/\partial t$. In the present study, the temporal envelope of $\Lambda_{\rho e_t}(\boldsymbol{x}, t)$ is thus defined in order for the term $\partial\Lambda_{\rho e_t}/\partial t$ to produce a period of a sinusoid, which, because of the very high amplitude in the source region, steepens and evolves into an N-wave.

Appendix B. Reflection of a spherical wave by a speed-of-sound inhomogeneity

In the model developed in § 4 to analyse the partial reflections, the pressure perturbation p' is governed by the wave equation

$$\frac{\partial^2 p'}{\partial x_1^2}+\frac{\partial^2 p'}{\partial x_2^2}+\bar{\rho}(x_3)\frac{\partial}{\partial x_3}\left(\frac{1}{\rho(x_3)}\frac{\partial p'}{\partial x_3}\right)-\frac{1}{\bar{c}^2(x_3)}\frac{\partial^2 p'}{\partial t^2}=-F(t)\delta(\boldsymbol{x}), \tag{B 1}$$

where the profiles of the speed of sound and the density vary only in the inhomogeneous layer located between the altitudes x_{3wb} and x_{3wt}. Taking the Fourier transform

$$\hat{p}'(k_1,k_2,x_3,\omega)=\iiint_{-\infty}^{+\infty} p'(x_1,x_2,x_3,t)\mathrm{e}^{-\mathrm{i}(k_1x_1+k_2x_2-\omega t)}\,\mathrm{d}x_1\,\mathrm{d}x_2\,\mathrm{d}t \tag{B 2}$$

yields the depth-separated Helmholtz equation

$$\bar{\rho}(x_3)\frac{\mathrm{d}}{\mathrm{d}x_3}\left(\frac{1}{\rho(x_3)}\frac{\mathrm{d}\hat{p}'}{\mathrm{d}x_3}\right)+\left(\frac{\omega^2}{\bar{c}^2(x_3)}-k_1^2-k_2^2\right)\hat{p}'=-\hat{F}(\omega)\delta(x_3). \tag{B 3}$$

For $x_3 \ll x_{3w}$, the medium is homogeneous and the pressure field $\hat{p}'(k_1,k_2,x_3,\omega)$ is given by

$$\hat{p}'(k_1,k_2,x_3,\omega)=\begin{cases}\alpha_1\mathrm{e}^{\mathrm{i}k_3x_3}+\alpha_2\mathrm{e}^{-\mathrm{i}k_3x_3}, & x_3>0\\ \beta_1\mathrm{e}^{\mathrm{i}k_3x_3}+\beta_2\mathrm{e}^{-\mathrm{i}k_3x_3}, & x_3<0,\end{cases} \tag{B 4}$$

where $k_3(k_1,k_2,\omega)=\sqrt{\omega^2/\bar{c}_\infty^2-k_1^2-k_2^2}$ is the vertical wavenumber and α_1, α_2, β_1 and β_2 are constants to be determined. First, the solution $\hat{p}'$ must behave as an outgoing wave as $x_3\to-\infty$. Hence, $\beta_1=0$. Moreover, as $x_3\to 0^+$, the ratio α_2/α_1 must tend to the reflection coefficient $\mathcal{R}_c$ for a plane wave of the form $\mathrm{e}^{\mathrm{i}(k_1x_1+k_2x_2+k_3x_3-\omega t)}$ propagating towards the inhomogeneity. In addition, since the function $\hat{p}'$ has to be continuous at $x_3=0$, the relation $\alpha_1+\alpha_2-\beta_2=0$ must be satisfied. Finally, by integrating equation (B 3) in the interval $[-x_{3\epsilon},+x_{3\epsilon}]$ and by taking the limit for $x_{3\epsilon}\to 0$, the following relation is obtained:

$$\lim_{x_3\to 0^+}\frac{\mathrm{d}\hat{p}'}{\mathrm{d}x_3}-\lim_{x_3\to 0^-}\frac{\mathrm{d}\hat{p}'}{\mathrm{d}x_3}=-\hat{F}, \tag{B 5}$$

which yields the condition

$$\alpha_1-\alpha_2+\beta_2=\frac{\mathrm{i}\hat{F}}{k_3}. \tag{B 6}$$

The solution $\hat{p}'$ can be finally written as

$$\hat{p}'(k_1,k_2,x_3,\omega)=\frac{\mathrm{i}\hat{F}(\omega)}{2k_3(k_1,k_2,\omega)}\left[\mathrm{e}^{\mathrm{i}k_3(k_1,k_2,\omega)|x_3|}+\mathcal{R}_c\mathrm{e}^{-\mathrm{i}k_3(k_1,k_2,\omega)x_3}\right]. \tag{B 7}$$

The first and second terms between brackets represent the incident field and the reflected wave, respectively. The function $p'(\boldsymbol{x},t)$ is then retrieved by taking the inverse Fourier transform

$$p'(\boldsymbol{x},t)=\frac{1}{8\pi^3}\iiint_{-\infty}^{+\infty}\hat{p}'(k_1,k_2,x_3,\omega)\mathrm{e}^{\mathrm{i}(k_1x_1+k_2x_2-\omega t)}\,\mathrm{d}k_1\,\mathrm{d}k_2\,\mathrm{d}\omega. \tag{B 8}$$

More specifically, the incident wave $p'_i(\boldsymbol{x}, t)$ is given by

$$p'_i(\boldsymbol{x}, t) = \frac{1}{8\pi^2} \int_{-\infty}^{+\infty} \hat{F}(\omega) \left[\iint_{-\infty}^{+\infty} \frac{\mathrm{i}\mathrm{e}^{\mathrm{i}(k_1 x_1 + k_2 x_2 + \mathrm{i}k_3(k_1, k_2, \omega)|x_3|)}}{2\pi k_3(k_1, k_2, \omega)} \, \mathrm{d}k_1 \, \mathrm{d}k_2 \right] \mathrm{e}^{-\mathrm{i}\omega t} \, \mathrm{d}\omega. \tag{B 9}$$

As shown by Frisk (1994), the term between brackets is equal to the Green function for the Helmholtz equation in a three-dimensional homogeneous free space, $\mathrm{e}^{\mathrm{i}\omega\|\boldsymbol{x}\|/\bar{c}_\infty}/\|\boldsymbol{x}\|$. It follows that

$$p'_i(\boldsymbol{x}, t) = \frac{1}{4\pi\|\boldsymbol{x}\|} \int_{-\infty}^{+\infty} \frac{\hat{F}(\omega)}{2\pi} \mathrm{e}^{-\mathrm{i}\omega(t - \|\boldsymbol{x}\|/\bar{c}_\infty)} \, \mathrm{d}\omega = \frac{F(t - \|\boldsymbol{x}\|/\bar{c}_\infty)}{4\pi\|\boldsymbol{x}\|}. \tag{B 10}$$

The reflected wave $p'_r(\boldsymbol{x}, t)$ can be finally expressed as

$$p'_r(\boldsymbol{x}, t) = \frac{1}{8\pi^2} \int_{-\infty}^{+\infty} \left[\iint_{-\infty}^{+\infty} \frac{\mathrm{i}\hat{F}(\omega)\mathcal{R}_c \mathrm{e}^{\mathrm{i}(k_1 x_1 + k_2 x_2 - \mathrm{i}k_3(k_1, k_2, \omega) x_3)}}{2\pi k_3(k_1, k_2, \omega)} \, \mathrm{d}k_1 \, \mathrm{d}k_2 \right] \mathrm{e}^{-\mathrm{i}\omega t} \, \mathrm{d}\omega. \tag{B 11}$$

REFERENCES

ASSINK, J., WAXLER, R. & VELEA, D. 2017 A wide-angle high Mach number modal expansion for infrasound propagation. *J. Acoust. Soc. Am.* **141** (3), 1781–1792.

ASSINK, J. D., LE PICHON, A., BLANC, E., KALLEL, M. & KHEMIRI, L. 2014 Evaluation of wind and temperature profiles from ECMWF analysis on two hemispheres using volcanic infrasound. *J. Geophys. Res. Atmos.* **119**, 8659–8683.

ASSINK, J. D., WAXLER, R., FRAZIER, W. G. & LONZAGA, J. 2013 The estimation of upper atmospheric wind model updates from infrasound data. *J. Geophys. Res. Atmos.* **118**, 10707–10724.

BATCHELOR, G. K. 2012 *An Introduction to Fluid Dynamics*. Cambridge University Press.

BERGMANN, P. G. 1946 The wave equation in a medium with a variable index of refraction. *J. Acoust. Soc. Am.* **17** (4), 329–333.

BERLAND, J., BOGEY, C. & BAILLY, C. 2007 High-order, low dispersive and low dissipative explicit schemes for multi-scale and boundary problems. *J. Comput. Phys.* **224** (2), 637–662.

BERRY, A. & DAIGLE, G. A. 1988 Controlled experiments of the diffraction of sound by a curved surface. *J. Acoust. Soc. Am.* **83** (6), 2047–2058.

BERTIN, M., MILLET, C. & BOUCHE, D. 2014 A low-order reduced model for the long-range propagation of infrasounds in the atmosphere. *J. Acoust. Soc. Am.* **136**, 37–52.

BLANC-BENON, P., DALLOIS, L. & JUVÉ, D. 2001 Long-range sound propagation in a turbulent atmosphere within the parabolic approximation. *Acta Acust.* **87**, 659–669.

BOGEY, C. & BAILLY, C. 2002 Three-dimensional non-reflective boundary conditions for acoustic simulations: far-field formulation and validation test cases. *Acta Acust. Unit. Ac.* **88**, 463–471.

BOGEY, C. & BAILLY, C. 2004 A family of low dispersive and low dissipative explicit schemes for noise computations. *J. Comput. Phys.* **194** (1), 194–214.

BOGEY, C., CACQUERAY, N. D. & BAILLY, C. 2009 A shock-capturing methodology based on adaptive spatial filtering for high-order nonlinear computations. *J. Comput. Phys.* **228**, 1447–1465.

BRACHET, N., BROWN, D., BRAS, R. LE, CANSI, Y., MIALLE, P. & COYNE, J. 2010 Monitoring the Earth's atmosphere with the global IMS infrasound network. In *Infrasound Monitoring for Atmospheric Studies* (ed. A. Le Pichon, E. Blanc & A. Hauchecorne), pp. 77–118. Springer.

CANDEL, S. M. 1977 Numerical solution of conservation equations arising in linear wave theory: application to aeroacoustics. *J. Fluid Mech.* **83** (3), 465–493.

CHUNCHUZOV, I. P., KULICHKOV, S. N. & FIRSTOV, P. P. 2013 On acoustic n-wave reflections from atmospheric layered inhomogeneities. *Izv. Atmos. Ocean. Phys.* **49** (3), 258–270.

CHUNCHUZOV, I. P., KULICHKOV, S. N., POPOV, O. E. & HEDLIN, M. 2014 Modeling propagation of infrasound signals observed by a dense seismic network. *J. Acoust. Soc. Am.* **135** (1), 38–48.

CHUNCHUZOV, I. P., KULICHKOV, S. N., POPOV, O. E., PEREPELKIN, V. G., VASILEV, A. P., GLUSHKOV, A. I. & FIRSTOV, P. P. 2015 Characteristics of a fine vertical wind-field structure in the stratosphere and lower thermosphere according to infrasonic signals in the zone of acoustic shadow. *Izv. Atmos. Ocean. Phys.* **51** (1), 57–74.

CHUNCHUZOV, I. P., KULICHKOV, S. N., POPOV, O. E., WAXLER, R. & ASSINK, J. 2011 Infrasound scattering from atmospheric anisotropic inhomogeneities. *Izv. Atmos. Ocean. Phys.* **47** (5), 540–557.

DEL PINO, S., DESPRÉS, B., HAVÉ, P., JOURDREN, H. & PISERCHIA, P. F. 2009 3D finite volume simulation of acoustic waves in the earth atmosphere. *Comput. Fluids* **38**, 765–777.

DROB, D. P., PICONE, J. M. & GARCÉS, M. 2003 Global morphology of infrasound propagation. *J. Geophys. Res. Atmos.* **108** (D21), 4680.

EVERS, L. G. & HAAK, H. W. 2010 The characteristics of infrasound, its propagation and some early history. In *Infrasound Monitoring for Atmospheric Studies* (ed. A. Le Pichon, E. Blanc & A. Hauchecorne), pp. 3–27. Springer.

FRISK, G. V. 1994 *Ocean and Seabed Acoustics. A Theory of Wave Propagation*. PTR Prentice Hall.

GAINVILLE, O., BLANC-BENON, P., BLANC, E., ROCHE, R., MILLET, C., LE PIVER, F., DESPRES, B. & PISERCHIA, P. F. 2010 Misty picture: a unique experiment for the interpretation of the infrasound propagation from large explosive sources. In *Infrasound Monitoring for Atmospheric Studies* (ed. A. Le Pichon, E. Blanc & A. Hauchecorne), pp. 575–598. Springer.

GALLIN, L.-J., RÉNIER, M., GAUDARD, E., FARGES, T., MARCHIANO, R. & COULOUVRAT, F. 2014 One-way approximation for the simulation of weak shock wave propagation in atmospheric flows. *J. Acoust. Soc. Am.* **135**, 2559–2570.

GODIN, O. A. 2002 An effective quiescent medium for sound propagating through an inhomogeneous, moving fluid. *J. Acoust. Soc. Am.* **112** (4), 1269–1275.

DE GROOT-HEDLIN, C. 2012 Nonlinear synthesis of infrasound propagation through an inhomogeneous, absorbing atmosphere. *J. Acoust. Soc. Am.* **132**, 646–656.

DE GROOT-HEDLIN, C. 2016 Long-range propagation of nonlinear infrasound waves through an absorbing atmosphere. *J. Acoust. Soc. Am.* **139**, 1565–1577.

DE GROOT-HEDLIN, C. 2017 Infrasound propagation in tropospheric ducts and acoustic shadow zones. *J. Acoust. Soc. Am.* **142** (4), 1816–1827.

DE GROOT-HEDLIN, C., HEDLIN, M. A. H. & WALKER, K. 2011 Finite difference synthesis of infrasound propagation through a windy, viscous atmosphere: application to a bolide explosion detected by seismic networks. *Geophys. J. Intl* **185**, 305–320.

INOUE, Y. & YANO, T. 1997 Propagation of strongly nonlinear plane N-waves. *J. Fluid Mech.* **341**, 59–76.

JACOBSEN, D. A. & SENOCAK, I. 2013 Multi-level parallelism for incompressible flow computations on GPU clusters. *Parallel Comput.* **39** (1), 1–20.

JENSEN, F. B., KUPERMAN, W. A., PORTER, M. B. & SCHMIDT, H. 2011 *Computational Ocean Acoustics*. Springer.

KULICHKOV, S. N. 2004 Long-range propagation and scattering of low-frequency sound pulses in the middle atmosphere. *Meteorol. Atmos. Phys.* **85**, 47–60.

LACANNA, G. & RIPEPE, M. 2013 Influence of near-source volcano topography on the acoustic wavefield and implication for source modeling. *J. Volcanol. Geotherm. Res.* **250**, 9–18.

LALANDE, J.-M., SÈBE, O., LANDÈS, M., BLANC-BENON, P., MATOZA, R. S., LE PICHON, A. & BLANC, E. 2012 Infrasound data inversion for atmospheric sounding. *Geophys. J. Intl* **190**, 687–701.

LE PICHON, A., BLANC, E., DROB, D., LAMBOTTE, S., DESSA, X., LARDY, M., BANI, P. & VERGNIOLLE, S. 2006 Infrasound monitoring of volcanoes to probe high-altitude winds. *J. Geophys. Res.* **110** (D13), 1–12.

LE PICHON, A., BLANC, E. & HAUCHECORNE, A. (Eds) 2010 *Infrasound Monitoring for Atmospheric Studies*. Springer Science + Business Media.

LE PICHON, A., CERANNA, L. & VERGOZ, J. 2012 Incorporating numerical modeling into estimates of the detection capabilities of the IMS infrasound network. *J. Geophys. Res.* **117** (D5).

LEKNER, J. 1987 *Theory of Reflection of Electromagnetic and Particle Waves*. Springer Science + Business Media.

LINGEVITCH, J. F., COLLINS, M. D. & SIEGMANN, W. L. 1999 Parabolic equations for gravity and acousto-gravity waves. *J. Acoust. Soc. Am.* **105**, 3049–3056.

LONZAGA, J. B., WAXLER, R. M., ASSINK, J. D. & TALMADGE, C. L. 2015 Modelling waveforms of infrasound arrivals from impulsive sources using weakly nonlinear ray theory. *Geophys. J. Intl* **200**, 1347–1361.

MARCHIANO, R., COULOUVRAT, F. & GRENON, R. 2003 Numerical simulation of shock wave focusing at fold caustics, with application to sonic boom. *J. Acoust. Soc. Am.* **114** (4), 1758–1770.

MARSDEN, O., BAILLY, C. & BOGEY, C. 2014 A study of infrasound propagation based on high-order finite difference solutions of the Navier–Stokes equations. *J. Acoust. Soc. Am.* **135**, 1083–1095.

OSTASHEV, V. E., SALOMONS, E. M., CLIFFORD, S. F., LATAITIS, R. J., WILSON, D. K., BLANC-BENON, P. & JUVÉ, D. 2001 Sound propagation in a turbulent atmosphere near the ground: a parabolic equation approach. *J. Acoust. Soc. Am.* **109**, 1894–1908.

PIERCE, A. D. 1985 *Acoustics: An Introduction to Its Physical Principles and Applications*. Acoustical Society of America.

PIERCE, A. D. 1990 Wave equation for sound in fluids with unsteady inhomogeneous flow. *J. Acoust. Soc. Am.* **87** (6), 2292–2299.

ROGERS, P. H. & GARDNER, J. H. 1980 Propagation of sonic booms in the thermosphere. *J. Acoust. Soc. Am.* **67** (1), 78–91.

SABATINI, R. & BAILLY, C. 2015 Numerical algorithm for computing acoustic and vortical spatial instability waves. *AIAA J.* **53** (3), 692–702.

SABATINI, R., MARSDEN, O., BAILLY, C. & BOGEY, C. 2016*a* A numerical study of nonlinear infrasound propagation in a windy atmosphere. *J. Acoust. Soc. Am.* **140**, 641–656.

SABATINI, R., MARSDEN, O., BAILLY, C. & GAINVILLE, O. 2015 Numerical simulation of infrasound propagation in the earth's atmosphere: study of a stratospherical arrival pair. *AIP Conf. Proc.* **1685** (1), 090002.

SABATINI, R., MARSDEN, O., BAILLY, C. & GAINVILLE, O. 2016*b* Characterization of absorption and non-linear effects in infrasound propagation using an augmented Burgers' equation. *Geophys. J. Intl* **207**, 1432–1445.

SALOMONS, E. M. 1998 Caustic diffraction fields in a downward refracting atmosphere. *J. Acoust. Soc. Am.* **104** (6), 3259–3272.

SALOMONS, E. M., BLUMRICH, R. & HEIMANN, D. 2002 Eulerian time-domain model for sound propagation over a finite-impedance ground surface: comparison with frequency-domain models. *Acta Acust. Unit. Ac.* **88**, 483–492.

SCOTT, J. F., BLANC-BENON, P. & GAINVILLE, O. 2017 Weakly nonlinear propagation of small-wavelength, impulsive acoustic waves in a general atmosphere. *Wave Motion* **72**, 41–61.

SUTHERLAND, L. C. & BASS, H. E. 2004 Atmospheric absorption in the atmosphere up to 160 km. *J. Acoust. Soc. Am.* **115** (3), 1012–1032.

SUTHERLAND, L. C. & BASS, H. E. 2006 Erratum: Atmospheric absorption in the atmosphere up to 160 km. *J. Acoust. Soc. Am.* **120** (5), 2985.

WAXLER, R. 2002 A vertical eigenfunction expansion for the propagation of sound in a downward-refracting atmosphere over a complex impedance plane. *J. Acoust. Soc. Am.* **112**, 2540–2552.

WAXLER, R. 2004 Modal expansions for sound propagation in the nocturnal boundary layer. *J. Acoust. Soc. Am.* **115**, 1437–1448.

WAXLER, R., ASSINK, J. & VELEA, D. 2017 Modal expansions for infrasound propagation and their implications for ground-to-ground propagation. *J. Acoust. Soc. Am.* **141** (2), 1290–1307.

WHITHAM, G. B. 1974 *Linear and Nonlinear Waves*. Wiley & Sons.